Research Square

Preprints are preliminary reports that have not undergone peer review.
They should not be considered conclusive, used to inform clinical practice,
or referenced by the media as validated information.

Investigation of the Behavior of Epoxy- and Lead-Bonded Mechanical Steel Stitching for Seismic Strengthening of Historical Stone Masonry Arches

Mohammad Manzoor Nasery

mnasery@ktu.edu.tr

Karadeniz Technical University: Karadeniz Teknik Universitesi https://orcid.org/0000-0003-3787-1355

Ali Kaya

Artvin Coruh Universitesi

Mohammad Saber Sadid

Sakarya Universitesi

Mohammad Bilal Jalali

Sakarya Universitesi

Research Article

Keywords: Kahramanmaraş earthquakes, Masonry arch, Mechanical Steel Stitching, Seismic strengthening, Harran Ulu Mosque

Posted Date: June 15th, 2026

DOI: https://doi.org/10.21203/rs.3.rs-9800809/v1

License: This work is licensed under a Creative Commons Attribution 4.0 International License.
Read Full License

Investigation of the Behavior of Epoxy- and Lead-Bonded Mechanical Steel Stitching for Seismic Strengthening of Historical Stone Masonry Arches

Mohammad Manzoor Nasery, *Dr.*
mnasery@ktu.edu.tr
Dynamica Mühendislik Co., 61010 Trabzon, Türkiye

Ali Kaya, *Dr.*
akaya@artvin.edu.tr
Artvin Çoruh University, Department of Architecture, 08100, Artvin, Türkiye

Mohammad Saber Sadid, *Dr.*
saber.sadid@ogr.sakarya.edu.tr
Sakarya University, Department of Civil Engineering, 54050, Sakarya, Türkiye

Mohammad Bilal Jalali, *Dr.*
mohammadbilaljalali@gmail.com
Dynamica Mühendislik Co., 61010 Trabzon, Türkiye
Sakarya University, Department of Civil Engineering, 54050, Sakarya, Türkiye

Correspondence Address:
Mohammad Manzoor **Nasery***, Dr.*
Karadeniz Technical University,
Department of Civil Engineering,
61080, Trabzon, TURKEY.
E-mail: mnasery@ktu.edu.tr

Abstract

Historical stone masonry arches are highly vulnerable to seismic actions due to their limited tensile capacity, weak inter-block continuity, and susceptibility to out-of-plane instability. This study investigates the effectiveness of mechanical steel stitching with clamp-type connectors as a minimally invasive strengthening technique for historical stone arches, focusing on the effects of clamp arrangement and embedment material on structural performance. An integrated experimental and numerical methodology was adopted. First, the mechanical properties of cut-stone masonry and AISI 304 stainless steel clamps were characterized, and in-situ pull-out tests were conducted to compare lead- and epoxy-bonded anchorage systems. The results showed that epoxy-bonded clamps achieved an average pull-out capacity of 4.38 kN, approximately seven times higher than that of lead-bonded clamps. A finite element model of the pull-out test was then developed using a cohesive contact formulation, and the interface parameters were calibrated against the experimental load-displacement response, reproducing the peak load with an error of approximately 5%. The validated interface model was implemented in three-dimensional micro masonry arch models representing unreinforced, single-row mechanical steel stitching, and double-row stitching configurations. Dynamic analyses showed that the maximum absolute out-of-plane displacement decreased from approximately 28 mm in the unreinforced model to 15 mm and 12 mm in the single- and double-row stitching models, respectively. Finally, the proposed strategy was evaluated through a case study on the Harran Ulu Mosque entrance arches damaged during the 2023 Kahramanmaraş earthquakes. The maximum out-of-plane displacement decreased from approximately 260 mm to 195 mm in the clamp-enhanced model and to 135 mm in the buttressed configuration. Overall, the findings demonstrate that epoxy-bonded double-clamp steel stitching provides an effective and heritage-compatible strengthening strategy for historical stone masonry arches.

Keywords: Kahramanmaraş earthquakes, Masonry arch, Mechanical Steel Stitching, Seismic strengthening, Harran Ulu Mosque.

1. Introduction

Masonry arches stand as remarkable examples of historical engineering, reflecting the ingenuity and craftsmanship of past civilizations. [1,2]. Their curved geometry allows an efficient transfer of loads through compression, providing long-term durability under gravity forces. However, the inherent weakness of masonry structures against tensile and shear forces renders them highly vulnerable to seismic movements [3]. During earthquakes, differential movements between supports and inertial forces acting on arch segments can cause joints to open, crack, and arch stones to partially detach [4]. Such damage mechanisms often compromise both structural stability and historical authenticity. Strengthening approaches such as concrete overlay, fiber-reinforced polymer (FRP) jacket, or steel frames are effective in increasing strength but often conflict with conservation principles due to their invasive and irreversible nature [5]. Experimental investigations on masonry arches have similarly emphasized that, although strengthening interventions can substantially improve structural capacity, their applicability to heritage structures must be evaluated in relation to conservation compatibility and limited alteration of the original structural system [6]. Therefore, recent research has focused on developing compatible and minimally intrusive reinforcement techniques, such as mechanical clamps, dowels, and localized reinforcement systems, to enhance the seismic performance of masonry arches while preserving their original material and aesthetic characteristics [5-8].

Preservation of historic masonry monuments has gained increased attention in recent decades, not only to safeguard cultural heritage but also to ensure structural safety against natural hazards. Among the various reinforcement methods proposed, mechanical connectors such as dowels and clamps have been historically used to enhance the integrity of stone assemblies by restricting separation and improving load transfer between units. Related studies on connector-based masonry strengthening have also shown that metallic tie systems can improve inter-element continuity and significantly enhance resistance against out-of-plane failure mechanisms [9]. Recent experimental and numerical studies confirm that clamps significantly increase the tensile and shear resistance of masonry, thereby improving overall seismic performance [10-12]. Strengthening methods implemented through the use of dowels and clamps substantially improve the structural integrity of stone arches, thereby contributing to a significant extension of their service life. In addition, such techniques are often considered more compatible with the authenticity of historic structures compared to modern interventions such as reinforced overlays or FRP composites.

The use of iron clamps and dowels as mechanical connectors in stone masonry structures has a long historical tradition, dating back to the Roman and Byzantine periods. In these eras, iron or bronze clamps were often embedded in molten lead to secure adjacent stone blocks in arches, domes, and walls, effectively enhancing the tensile resistance of the joints and preventing differential displacement between blocks. During the Ottoman period, this technique evolved into a refined construction practice widely employed in monumental buildings such as mosques, bridges, and fortification walls, where iron clamps and dowels were used to ensure both structural continuity and durability under dynamic actions such as earthquakes [2]. These historical practices represent some of the earliest examples of mechanical strengthening methods, inspiring modern heritage-compatible reinforcement techniques for masonry structures.

Numerous studies have demonstrated that the Finite Element Method (FEM) is an effective tool for assessing the structural behavior of historical stone arches. This method enables analytical investigation of the complex geometry, material heterogeneity, and contact behavior inherent to masonry structures. FEM allows for a detailed evaluation of load-bearing capacity, stress distribution, and crack propagation of arches under both static loads (self-weight, settlement effects) and dynamic loads (earthquake, wind, vibration) [13-15]. Recent studies on historical masonry complexes have further demonstrated that nonlinear numerical modeling, including both continuous and discontinuous approaches, is essential for capturing localized damage evolution, crack propagation, sliding mechanisms, and the emergence of collapse modes under seismic excitation [16-19]. For instance, studies on historical stone bridge arches have revealed that nonlinear finite element analyses can accurately predict crack propagation mechanisms and collapse behavior [20]. Similarly, research focusing on the seismic performance of cultural heritage structures has shown that accurately defining contact interfaces and material parameters during the modeling process significantly enhances the reliability of structural response predictions [15]. Therefore, FEM has become a non-invasive and reliable approach widely employed for assessing the current damage state of historical arches and virtually testing potential strengthening scenarios.

Although the retrofitting of masonry arches is crucial for the preservation of historical structures, studies focusing on their seismic behavior remain relatively limited. Nevertheless, recent research has provided valuable insights into their response mechanisms and the effectiveness of various strengthening strategies. Çavuşlu and Ülger [2] conducted a comprehensive study on the Batıayaz Bridge to enhance the seismic resistance of historic stone

bridges. The study examined the structural effects of replacing the traditional iron clamps used between stones in the arch section with alternative FRP connection elements. The researchers performed FLAC3D finite difference analyses on models reinforced with both FRP and metal clamp-stud systems, using experimentally determined mechanical properties and stiffness values in these analyses. The results showed that both connection types significantly improved the seismic performance of the bridge, but that FRP connection elements offered a more advantageous solution for long-term strengthening due to their corrosion resistance. Tanrıverdi and Yavuz [10] investigated the effect of anchor depth on the load-bearing capacity of masonry walls both experimentally and numerically. Four-point bending tests conducted on eight different wall specimens showed that the use of anchors increased the load-bearing capacity by at least 10.53%. The study determined that an embedment depth of approximately 30% of the stone height provided optimum performance, while exceeding this ratio by 60% resulted in a decrease in capacity. The findings revealed that the dimensioning of the tie is a critical parameter in the strength and ductility behaviour of masonry structures. Çavuşlu and Ulger [12] investigated the effect of clamp and dowel systems in historic stone bridges on seismic performance both experimentally and numerically. The study was conducted on the Plaka Bridge, and a nonlinear model that realistically represents the behavior of the interface between stones was proposed. Stiffness values determined through experimental testing were used in 3D Finite Difference Model (FDM) to evaluate the bridge's response under the 2023 Kahramanmaraş earthquakes. Findings showed that the clamp and dowels significantly reduced displacements and stress concentrations, thereby markedly enhancing structural integrity and seismic resistance. Ural and Uslu [21] experimentally investigated the effect of metal ties and dowels used in historic stone walls on shear behaviour. In the study, 12 different stone wall specimens and an unreinforced reference wall were subjected to shear loading. The experimental parameters considered were the length of the fasteners, the number of fasteners, and the number of dowels. The results clearly demonstrated the effects of different connection configurations on the load-bearing capacity and failure mechanism. In another study, an experimental investigation was conducted on the reinforcement of lightweight masonry elements (aerated concrete walls) with ties [22]. In this study, six aerated concrete wall specimens were tested under diagonal pressure; one of these was a reference (unreinforced), while the other five were reinforced with different tie and anchor arrangements. The experimental findings showed that the fastener systems, consisting of Ø12 ribbed steel bars and welded plates, significantly increased the rigidity, energy absorption capacity, and load-bearing

capacity by enhancing the bond strength between the aerated concrete blocks. Furthermore, the reinforced specimens exhibited more ductile behaviour compared to the reference walls.

As these studies have also demonstrated, although significant progress has been made in recent years regarding the seismic strengthening of historic stone arches, the effects of mechanical connection elements (e.g., clamps and dowels) on the dynamic behavior of these structures have not yet been sufficiently clarified. Although a large part of the existing literature has focused on different strategies such as steel reinforcement, FRP composites, post-tensioning systems, and base isolation in the repair and reinforcement of masonry structures [23-35], the specific contribution of mechanical connection elements to the seismic performance of stone arches has been addressed only to a limited extent. Furthermore, a significant portion of existing research has been limited to small-scale walls or simplified numerical analyses; consequently, there are notable gaps in the literature regarding full-scale experimental validations and three-dimensional non-linear models.

Furthermore, the type of filling material used for embedding clamps into stone is a critical parameter that directly affects the connection performance. Traditionally, lead fillings have been preferred in historical structures, as lead can create a mechanical bond with stone surfaces without causing chemical reactions. However, since molten lead solidifies rapidly during application, it often fails to completely fill the gaps and provides insufficient adhesion, particularly on inclined stone surfaces such as arches. This limitation indicates that lead fillings are mechanically inadequate for such applications. In contrast, epoxy-based materials are now considered a modern alternative due to their high adhesion properties, workability, and controllable curing process. Nevertheless, comprehensive experimental and numerical studies comparing the structural behavior of epoxy and lead fillings at the stone–clamp interface remain scarce in the literature. Existing research mainly focuses on the performance of chemical or epoxy anchors in masonry structures, demonstrating strong adhesion between epoxy and stone and quantifying the relationship between embedment depth and anchorage capacity; however, a systematic comparison with lead has not yet been presented [36]. Therefore, the present study aims to comparatively investigate the effects of these two filling materials on the load-bearing capacity and stiffness behavior of stone arches.

The central objective of this study is to quantify the contribution of mechanical clamps to the seismic response of stone masonry arches by examining their effects on stiffness, deformation capacity, and failure mechanisms under lateral loading. Furthermore, the study investigates the role of embedment materials, particularly lead and epoxy, in governing the stone–clamp

interface behavior, including normal and shear bond characteristics, contact stiffness, and load-transfer efficiency. By integrating controlled laboratory tests with nonlinear finite element simulations, the research aims to establish a more accurate representation of the clamp–stone interaction and to determine how variations in interface properties influence the global structural performance of the arch system. The overall research methodology, including material characterization, pull-out testing, finite element calibration, arch micro-modeling, and the Harran Ulu Mosque entrance arch case study, is summarized in Fig. 1. These findings are expected to inform the development of mechanically compatible and performance-oriented strengthening strategies for historic masonry arches. Fig. 2 shows that clamps are used as metal connectors in minarets, walls, and bridges in historical masonry structures.

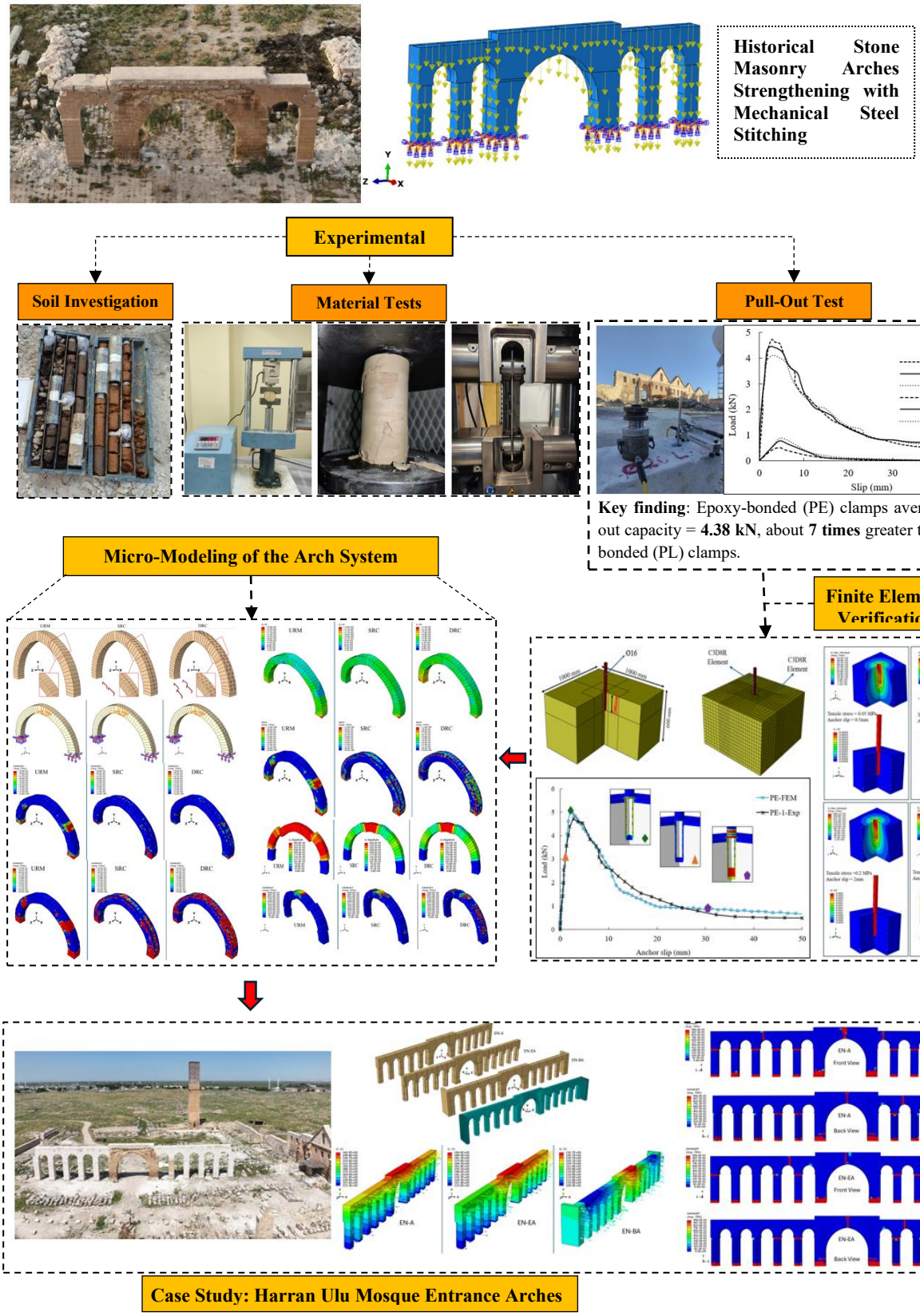


Figure 1. Flow chart of the study



Figure 2. The use of steel clamps as mechanical connectors in masonry structures

2. Structural Mechanics of Connections and Embedment Materials in Masonry Arches

Mechanical clamps serve as essential devices for maintaining continuity between individual blocks and ensuring the stability of the arch and spandrel regions. Typically fabricated from high-strength metals, these clamps are embedded within the masonry to generate a secure mechanical interlock capable of restraining relative movement under both gravitational and lateral loads. Their primary structural function is to prevent separation and sliding along bedding joints, thereby enhancing tensile resistance an otherwise deficient property of stone and improving the deformation capacity of the masonry assemblage. When properly positioned within the masonry fabric, clamps facilitate efficient transfer of loads across adjoining units, stabilize the intrados and extrados surfaces of the arch, and restrict the formation and propagation of critical hinge mechanisms during seismic excitation. Beyond their role in local connection behavior, clamps substantially influence the global response of masonry bridges by promoting structural homogeneity and reducing differential displacements along the arch barrel. The effectiveness of these elements, however, depends strongly on their material properties, geometric configuration, and installation quality, all of which determine the degree of bond that can be mobilized at the stone-clamp interface. Consequently, a thorough understanding of clamp mechanics is indispensable for interpreting the load-carrying mechanism of historic stone arches and for designing compatible strengthening strategies that preserve both their structural and architectural integrity.

In addition to the mechanical role of clamps, the type of embedment material used to secure them within the masonry plays a decisive role in the overall effectiveness of the connection. Traditional lead fillings, while historically preferred for their ease of casting and mechanical seating properties, exhibit inherently low bonding capacity, which limits their performance particularly in inclined or irregular stone surfaces commonly found along the intrados and extrados of arches. In such regions, molten lead often solidifies prematurely, preventing full penetration into the voids and resulting in insufficient confinement of the clamp. By contrast, epoxy-based fillers offer markedly higher adhesion strength and superior compatibility with uneven geometries, enabling more reliable anchorage where enhanced mechanical interlock is required. In relatively flat or horizontal masonry zones, lead may still function adequately, as the bonding demand is lower. However, under significant lateral displacement, the structural contribution of filler materials diminishes, making the limitations of lead more evident. Given its high adhesion capacity and ability to deliver the desired mechanical interaction at the stone–clamp interface, epoxy can therefore be considered a more suitable filler material for the strengthening of arch stones.

In the present study, the structural role of clamp connections and their embedment materials is investigated through a comprehensive numerical framework supported by material and soil characterization tests. To ensure realistic modeling inputs, laboratory experiments were conducted on stone specimens and foundation soils representative of those found in the entrance arch of the historic Harran Ulu Mosque in Sanliurfa, Türkiye. These experimentally derived parameters were then implemented in a series of independent numerical models to systematically examine the mechanical response of masonry arches strengthened with metal clamps under various loading conditions. Finally, a case-study analysis was performed by constructing a detailed finite element model of the actual entrance arch of the Harran Ulu Mosque, enabling an assessment of its seismic behavior and providing a direct comparison with the generalized numerical models. This multiscale approach allows for a rigorous evaluation of clamp efficiency and the influence of embedment materials within both idealized and real structural configurations.

3. Regional Seismicity and the 2023 Kahramanmaraş Earthquake Sequence

Due to its location in the interaction zone of the Eurasian, African, and Arabian plates, Türkiye is a country with a high seismic risk. The study area is located in southeastern Türkiye, a region characterized by high seismic activity due to its proximity to major active fault systems

governing the Anatolian plate dynamics (Fig. 3). The regional seismotectonic setting is primarily controlled by the interaction of the East Anatolian Fault Zone (EAFZ), the Dead Sea Fault Zone (DSFZ), and associated secondary fault segments, which collectively generate significant seismic hazard. These tectonic structures have been responsible for numerous destructive earthquakes throughout historical and instrumental records, posing a substantial risk to both modern and heritage structures.

On 6 February 2023, the region was severely affected by a sequence of catastrophic Kahramanmaras earthquakes, initiated by a moment magnitude Mw 7.7 (centered in Pazarcık district) mainshock followed by a Mw 7.6 (centered in Elbistan district) event occurring approximately nine hours later. This rare doublet earthquake sequence produced exceptionally strong ground motions over a wide area, resulting in extensive damage to masonry structures, particularly those lacking adequate tensile resistance and ductility. The intensity and duration of shaking revealed critical vulnerabilities in historical stone constructions, including arches and vault systems, where loss of connectivity and sliding between masonry units were observed. Details of the Kahramanmaraş earthquake sequence, including major aftershocks, are listed in Table 1.

Table 1. Seismic data related to the Kahramanmaraş earthquake sequence [38]

Date	Time	Latitude (°)	Longitude (°)	Depth (km)	Mw
Pazarcık earthquake					
06.02.2023	01:17:32	37.288	37.043	8.6	7.7
Nurdağı earthquake					
06.02.2023	01:28:16	37.304	36.920	6.2	6.6
Elbistan earthquake					
06.02.2023	10:24:47	38.089	37.239	7.0	7.6
Yayladağı earthquake					
20.02.2023	17:04:27	36.037	36.021	21.73	6.4

During the 6 February 2023 Kahramanmaraş earthquake sequence, strong ground motion records from both the main events and subsequent aftershocks were obtained from multiple seismic stations operated by the Disaster and Emergency Management Authority (AFAD) [38]. Analysis of these records indicates that the Pazarcık mainshock generated exceptionally intense shaking, with a maximum peak ground acceleration of 2.2 g in the east-west (E-W) direction at the Pazarcık station (No. 4614) (Fig. 4). Notably, the north-south (N-S) component exhibited a

similarly extreme acceleration level of approximately 2.1 g. Furthermore, the vertical (U-D) component reached values as high as 1.9 g, far exceeding levels typically assumed in conventional seismic design. Vertical ground motions are often considered secondary or substantially lower than horizontal components; however, the recorded data from this earthquake sequence demonstrate that vertical accelerations can attain magnitudes close to those of horizontal motions. Such pronounced vertical excitation is particularly critical for historical masonry structures, slender structural elements (e.g., arches), and mechanical connections, where it may activate damage mechanisms that are not commonly addressed in standard design and assessment procedures.

The response spectra obtained for all motion components, particularly at short vibration periods, clearly highlight the severe damage potential of the earthquake. These results demonstrate that seismic performance assessments should explicitly account for the combined effects of the E-W, N-S, and vertical (U-D) components, especially in the case of heritage or non-engineered structures where vertical load-transfer mechanisms and redundancy are often limited [15].

As discussed earlier, the proposed strengthening approach is evaluated through numerical analyses performed on the model of the entrance arches of the Harran Ulu Mosque. Within this framework, acceleration records obtained from two strong-motion stations located in close proximity to the mosque complex (Akçakale and Haliliye) during the 6 February 2023 Kahramanmaraş-Pazarcık earthquake were examined. The three orthogonal components of ground motion (E-W, N-S, and vertical) were analyzed in terms of both peak ground acceleration (PGA) and response spectra to capture the directional characteristics and frequency-dependent nature of the seismic input. Among the selected stations, the Haliliye station (No. 6305), which is geographically closer to Harran, recorded a maximum PGA of approximately 0.12 g. Although this level of ground acceleration may be considered moderate from a conventional design perspective, it is particularly significant for unreinforced stone arch systems, where stability relies on compressive load transfer and limited deformation capacity. In such structures, even moderate seismic demands can induce amplified dynamic responses, especially when the dominant frequencies of ground motion coincide with the natural vibration characteristics of the arches, potentially leading to loss of equilibrium and localized damage.

As illustrated in Figs. 5 and 6, the response spectra corresponding to the horizontal ground-motion components (E-W and N-S) significantly exceed the DD-2 design spectrum specified in the Turkish Building Earthquake Code (TBEC-2018) [40] within the period range of approximately 0.3-1.0 s. This interval closely aligns with the fundamental vibration periods

commonly observed in historical masonry arch systems, indicating a heightened susceptibility to resonance-induced amplification. Such spectral exceedance suggests that unreinforced stone arches may experience amplified inertial forces, leading to increased thrust demand and potential loss of stability. In addition, the vertical (U-D) component, which is often underestimated in conventional seismic assessments, exhibits spectral acceleration values reaching approximately 0.15 g at short periods. This level of vertical excitation is considered unusually high and may trigger complex damage mechanisms in stone arches, including degradation of mortar cohesion, separation at voussoir interfaces, and localized cracking near arch-spandrel transitions. The DD-1, DD-2, DD-3, and DD-4 design spectra shown for the Akçakale Station (Fig. 5) and Haliliye Station (Fig. 6) were derived from the official AFAD seismic hazard map. In this context, DD-1 corresponds to the Maximum Considered Earthquake with a 2% probability of exceedance in 50 years (return period of 2475 years), while DD-2 represents the design-level earthquake with a 10% probability of exceedance in 50 years (475-year return period). Similarly, DD-3 and DD-4 correspond to earthquakes with 50% and 68% probabilities of exceedance in 50 years, associated with return periods of 72 and 43 years, respectively.

The Harran district of Şanlıurfa, although located at a moderate distance from the epicentral area, experienced significant seismic demand due to long-period ground motion components and cumulative damage effects. The observed structural damage in historical masonry elements highlights the necessity of accurately characterizing regional seismicity when evaluating the seismic response and strengthening requirements of stone arches. In this context, the 2023 Kahramanmaraş earthquake sequence provides a valuable reference framework for assessing the effectiveness of mechanical connections and retrofit strategies considered in this study.

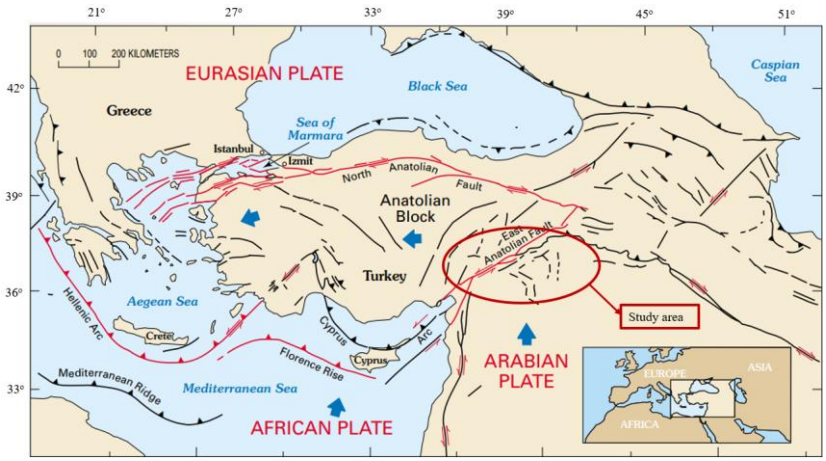


Figure 3. Tectonic map of Türkiye and location of the study area [37]

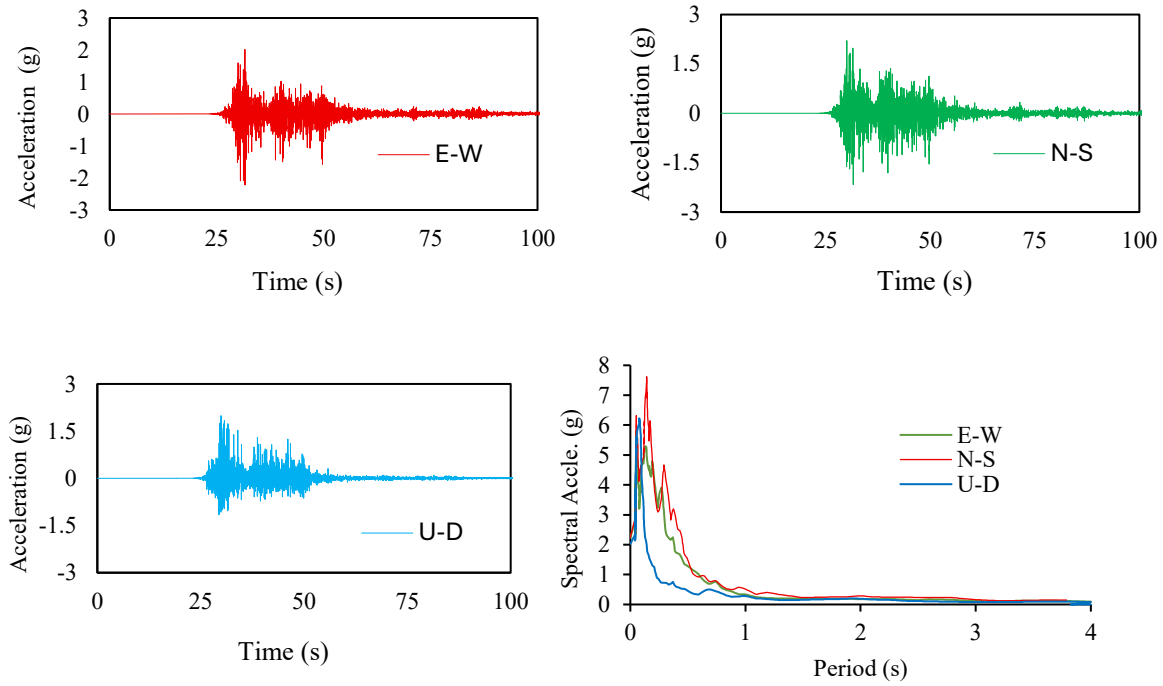


Figure 4. Acceleration time histories of the East-West (E-W), North-South (N-S), and vertical (U-D) components recorded at Pazarcık Station (4614) during the Kahramanmaraş-Pazarcık earthquake, together with the corresponding response spectra [39]

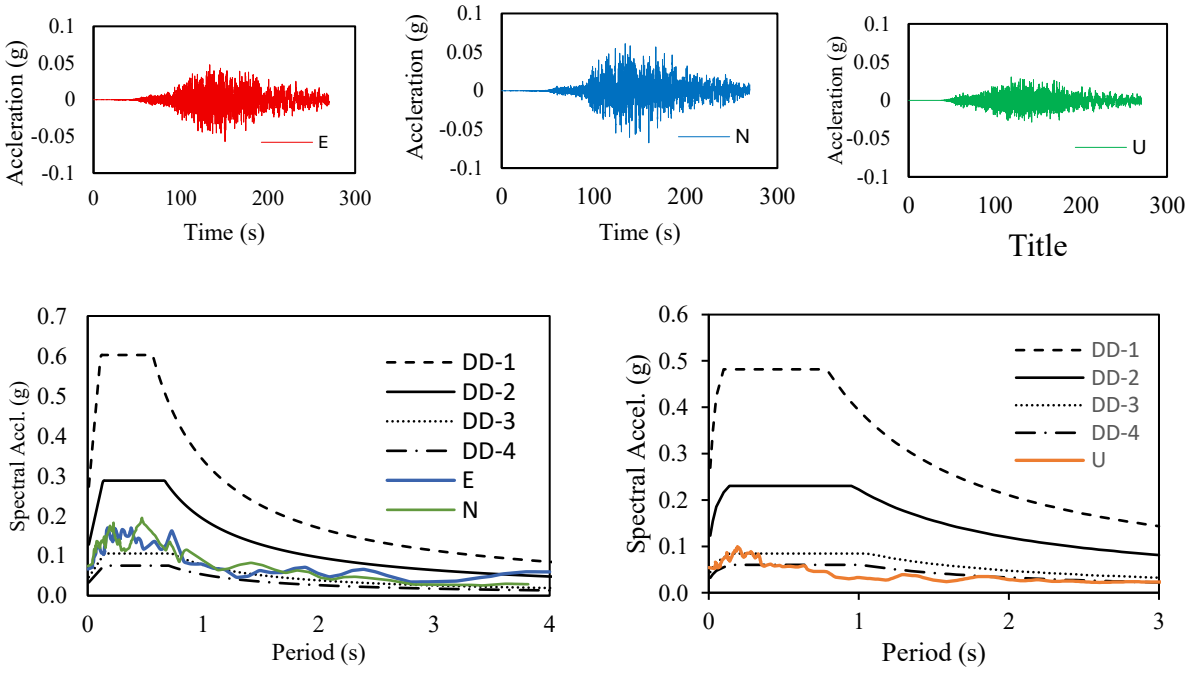


Figure 5. Acceleration records (E, N, and U components) from the Akçakale Station (6306) during the 6 February 2023 Kahramanmaraş–Pazarcık earthquake and the corresponding response spectra, compared with the design spectrum for the entrance arches of the Harran Ulu Mosque [39]

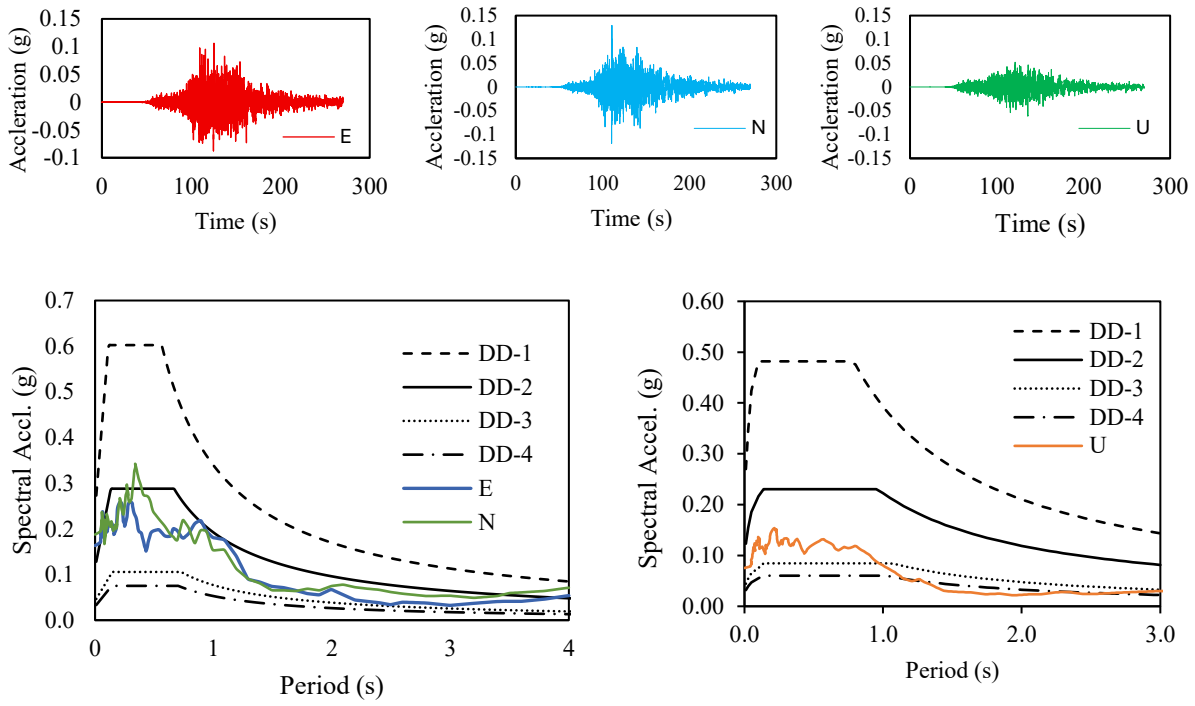


Figure 6. Acceleration records (E, N, and U components) from the Haliliye Station (6305) during the 6 February 2023 Kahramanmaraş–Pazarcık earthquake and the corresponding response spectra, compared with the design spectrum for the entrance arches of the Harran Ulu Mosque [39]

3.1. Soil Investigation and Geotechnical Characterization

A site-specific soil investigation was carried out to characterize the foundation conditions of the Harran Ulu Mosque arch structure. The study was performed in accordance with the TBEC-2018 [40] and included field investigations, geophysical surveys, and laboratory testing. Fig. 7 illustrates the core samples retrieved from the boreholes, which were examined to identify the subsurface soil and lithological conditions.

Within the scope of the field studies, one borehole (SK-1) was drilled to a depth of 15 m adjacent to the arch system. The borehole logs revealed a stratigraphic profile consisting of approximately 0.5 m of topsoil, underlain by blocky sand-gravel deposits extending to about 4.0 m, followed by sandy clay layers (CL-CH) down to the final drilling depth. Table 2 summarizes the lithological profile of borehole SK-1, including topsoil, blocky sand-gravel, and sandy clay layers. Standard Penetration Tests (SPT) were conducted at selected depths, yielding N-values ranging from 16 to 26, indicating medium-dense to stiff soil conditions.

To evaluate the dynamic properties of the subsurface, geophysical measurements were performed using Multichannel Analysis of Surface Waves (MASW) and Electrical Resistivity

Tomography (ERT). The MASW survey was conducted along a 48 m profile and provided shear-wave velocity information down to 30 m depth. Based on these measurements, the average shear-wave velocity (Vs30) was calculated as approximately 322 m/s, classifying the site as ZD soil type, corresponding to medium-dense sand–gravel and stiff clay layers according to TBEC-2018 [40]. The ERT results indicated generally low resistivity values, consistent with clayey soil units at depth.

Laboratory tests were carried out on disturbed and undisturbed samples obtained from the borehole, including water content, grain size distribution, Atterberg limits, unit weight determination, and unconsolidated–undrained triaxial compression tests. The results confirmed that the dominant subsurface material below the sand–gravel layer consists of plastic, stiff sandy clay (CL-CH).

No groundwater was encountered during drilling or geophysical investigations. Overall, the soil profile was found to be relatively homogeneous beneath the arch structure, providing a consistent foundation medium for structural analysis and seismic performance assessment.



Figure 7. Soil core samples collected during the geotechnical drilling program.

Table 2. Lithological profile identified from geotechnical borehole data

Borehole Code	Depth (m)	Lithology
SK-1	0.00-0.50	Topsoil
	0.50-4.00	Blocky Sand-Gravel
	4,00-15,00	Slightly Sandy Clay (CL-CH)

4. Experimental studies

4.1. Material Properties of Cut-Stone Masonry Arch

The entrance arches of the Harran Ulu Mosque are mainly composed of cut-stone masonry units bonded with lime-based mortar. In order to define the mechanical properties of the masonry material used in the numerical analyses, both site-specific experimental data and guideline-based engineering parameters were considered. This combined approach was adopted because the structural response of historical masonry arches is governed not only by the mechanical capacity of the stone blocks, but also by the condition of lime-based mortar joints, workmanship, inter-block contact, existing deterioration, and the continuity between adjacent units. This consideration is consistent with recent research on historical stone masonry, which emphasizes that the mechanical characterization of masonry assemblages is inherently uncertain and that unit-level material properties alone may not be sufficient to represent the global structural behavior of complete masonry systems [41].

Reported laboratory tests conducted on original cut-stone specimens taken from the Harran Ulu Mosque complex were used as a reference for the mechanical characterization of the stone material (Fig. 8). In that experimental program, cylindrical stone specimens were subjected to uniaxial compression and Brazilian splitting tensile tests. The measured compressive strength values of the original stone specimens were 8.35, 8.85, and 8.55 MPa, giving an average compressive strength of 8.58 MPa. The average unit weight was reported as 19.4 kN/m³. The average tensile strength obtained from Brazilian splitting tests was 0.72 MPa, and the modulus of elasticity was calculated as 4130.5 MPa using the FEMA [50] based relationship $E = 550 f_c$. Following this experimental characterization, the results of the uniaxial compressive strength and Brazilian splitting tensile strength tests carried out within the scope of the present study are presented in Tables 3 and 4, respectively. These results enable a direct comparison between the original and newly proposed stone materials in terms of their mechanical performance.



Figure 8. Experimental testing stages of the cut-stone material used in the entrance arches

Table 3. Uniaxial Compressive Strength Test Results

Property	Original Stone			New Stone		
Sample No	1	2	3	1	2	3
Sample Code	OS-1	OS-2	OS-3	NS-1	NS-2	NS-3
Diameter (mm)	54.10	54.25	53.95	53.80	54.10	53.75
Height (mm)	108.0	107.6	108.2	54.00	53.85	54.10
Unit Weight (kN/m³)	19.4	19.4	19.4	18.3	18.3	18.3
Area (mm²)	2298	2310	2285	2275	2290	2268
Failure Load (kN)	1920	2050	1985	2750	2890	3010
Compressive Strength (MPa)	8.35	8.85	8.55	12.30	13.10	13.75
Average Strength (MPa)	8.58			13.05		

Table 4. Brazilian Splitting Tensile Strength Test Results

Material Type	No	Sample Code	Diameter (mm)	Thickness (mm)	Sample Weight (g)	Failure Load (kg)	Tensile Strength (MPa)	Unit Weight (kg/m³)
Original	1	OS-1	54	28	130.5	170.2	0.72	1900
Stone	2	OS-2	54	27	115.2	160.4	0.68	1900
	3	OS-3	54	30	136.0	175.0	0.75	1900
Average							0.72	
New	1	NS-1	54	25	99.0	560.0	2.35	1780
Stone	2	NS-2	54	24	97.5	390.0	2.10	1780
	3	NS-3	54	24	98.0	470.0	2.28	1780
Average							2.24	

Although these experimental results provide important information on the intrinsic mechanical capacity of the original cut-stone units, the numerical analyses require material parameters that are representative of the overall behavior of the stone masonry arch system. Therefore, the

experimental stone strength values were not directly assigned as the compressive strength of the complete arch system. Instead, the final numerical parameters were selected in accordance with the recommendations of the Guideline for the Management of Earthquake Risks for Historical Structures [42], which provides representative values for historical masonry typologies and accounts for factors such as mortar quality, workmanship, and wall connectivity through correction coefficients.

A similar material definition strategy can be observed in the seismic assessment study of the Harran Ulu Mosque minaret by İzol et al. [51], where the initial material properties of the masonry components were assigned based on previous studies and literature-supported assumptions, while the compressive strength of masonry was evaluated using the formulation proposed by Tomaževič [43]. This demonstrates that, for historical masonry structures, experimentally measured unit properties and representative structural material parameters may be treated separately depending on the scale and objective of the numerical analysis.

In the present study, the values corresponding to cut-stone masonry walls were adopted for the entrance arch models. The tensile strength was taken as 10% of the corresponding compressive strength, which is a common assumption in the assessment of historical masonry structures [43]. The final material parameters used in the numerical analyses are summarized in Table 5. These parameters were used consistently in the numerical models to represent the mechanical behavior of the cut-stone masonry arch system.

Table 5. Material properties used in FEM analyses

	Modulus of Elasticity (MPa)	Poisson's Ratio (-)	Unit Volume Weight (kg/m^3)	Compressive Strength (MPa)	Tensile Strength (MPa)	Initial Shear Strength (MPa)
Stone Walls	2500	0.2	2100	2.50	0.25	0.093

4.2. Stainless Steel Clamp Material Test

In this study, the mechanical steel stitching method was adopted as the primary intervention technique for the reinforcement of structures similar to the historic stone arch systems located at the entrance to Harran Ulu Mosque. The fastening elements used in the strengthening approach were manufactured from 16 mm diameter ribbed AISI 304 grade stainless steel. In this context, an experimental characterization program was conducted to reliably assess the mechanical performance and potential damage behavior of the steel material in question.

As part of the experimental study, the material's uniaxial tensile behavior was tested at room temperature in accordance with the ISO 6892-1 standard published by the International Organization for Standardization [46]. The tests were carried out under strain-controlled loading, and the material's elastic-plastic transition behavior and plastic deformation capacity were examined in detail. To ensure the reproducibility of the results, three specimens were tested.

The test setup and the damage morphologies observed in the specimens after tensile testing are presented in Fig. 9. The test results revealed that all specimens exhibited a necking behavior following a distinct yield plateau, and it was determined that the ultimate fracture occurred in a ductile manner. The obtained yield strength, ultimate tensile strength and elongation at break values are detailed in Table 6. Furthermore, the engineering stress-strain curves, representing the material's stress transfer capacity and deformation capability, are presented in Fig. 10.

The findings indicate that the AISI 304 stainless steel used exhibits high ductility and energy absorption capacity; consequently, the clamping elements employed within the mechanical stitching method minimize the risk of brittle fracture, thereby contributing to the preservation of structural integrity. This is of critical importance, particularly in terms of preventing sudden and brittle damage to mechanisms in historic masonry structures.

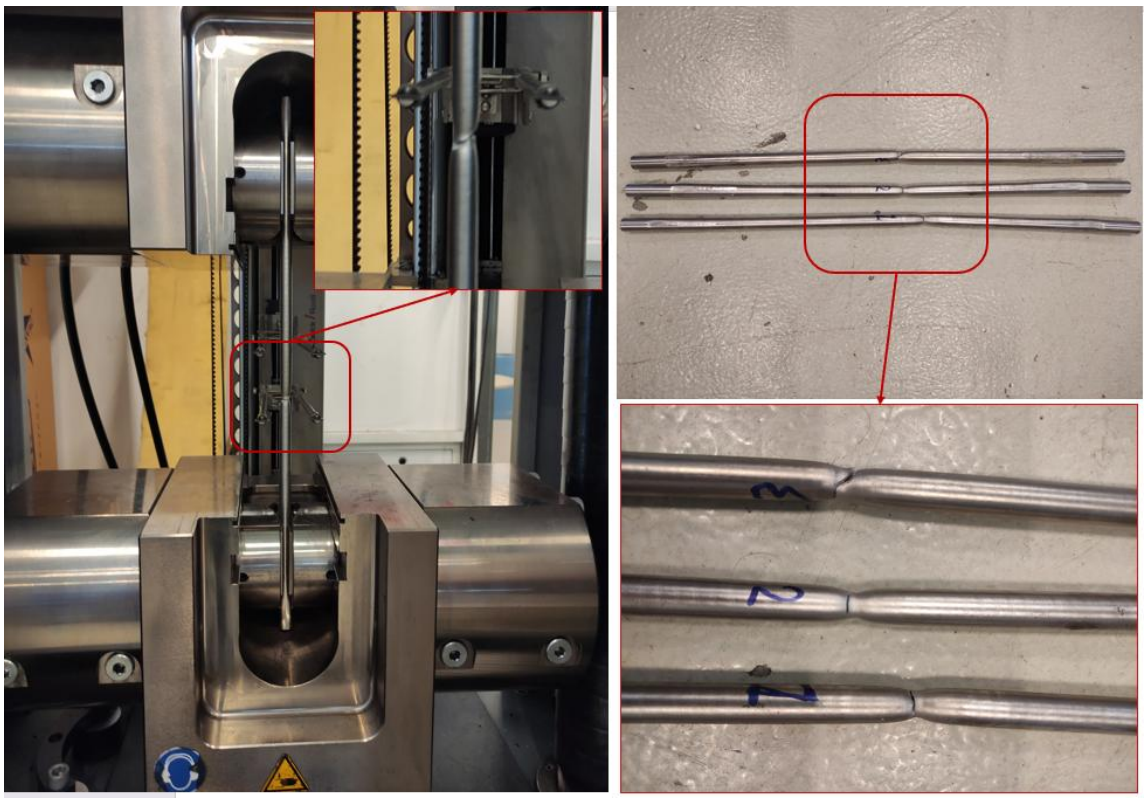


Figure 9. The material test setup and damage observed in samples after tensile testing

Table 6. Mechanical properties of AISI 304 stainless steel

Test item type	Unit area (mm^2)	0,2% Yield Strength (MPa)	Tensile Strength (MPa)	Percentage Total Extension at Fracture (%)
Sample 1	199,06	469	701	45,9
Sample 2	199,31	454	700	41,2
Sample 3	199,06	639	802	34,5

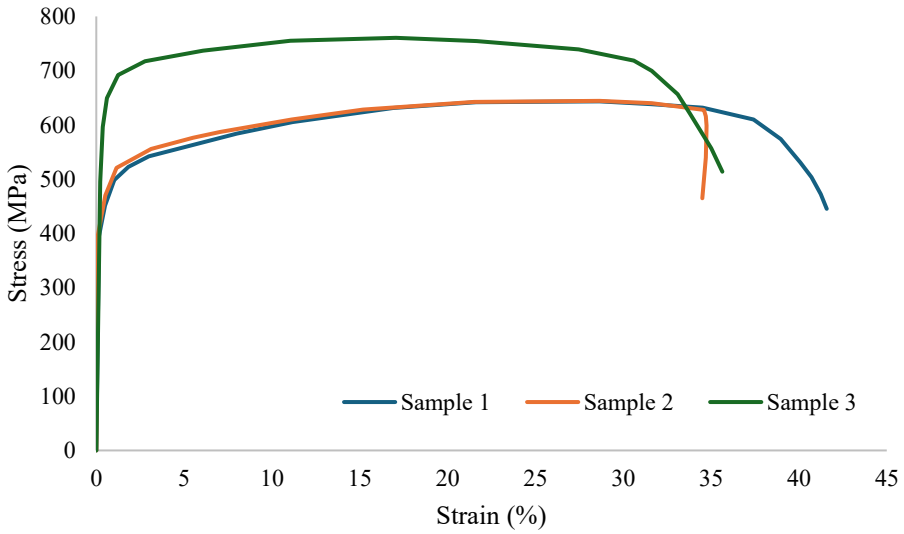


Figure 10. Engineering stress-strain curves of AISI 304 stainless steel

4.3. Pull-Out Tests for Mechanical Steel Stitching

In this study, the mechanical steel stitching method was selected as the primary reinforcement approach for the strengthening of structures similar to the stone arch systems located at the entrance to the Harran Ulu Mosque. In-situ axial pull-out tests were conducted on the steel stitches to evaluate the anchorage behavior of the proposed system and to compare the performance of different bonding materials.

A total of six anchors with a diameter of 16 mm were fabricated from ribbed AISI 304 stainless steel to enhance bond interaction. These anchors were divided into two groups, using lead and epoxy as bonding materials, with three specimens prepared for each case. The anchors were installed into cylindrical holes with a diameter of 40 mm and an embedment depth of 200 mm, drilled into representative stone blocks (Fig. 11). The holes were carefully cleaned to remove dust and debris, ensuring proper contact between the bonding material and the stone surface.

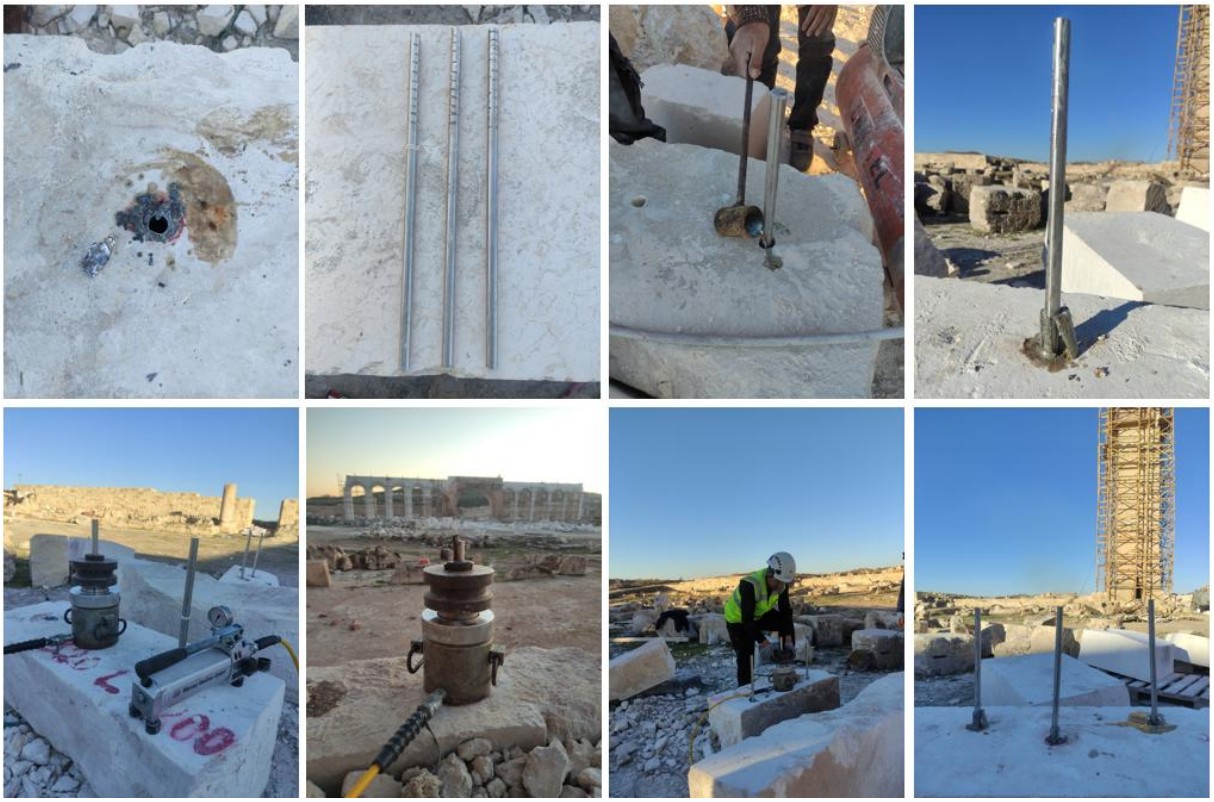


Figure 11. Field test views of mechanical steel stitches anchored using lead and epoxy.

For epoxy-based specimens, a two-component epoxy acrylate adhesive (Teknobond 401 W, compliant with EN 1504-6 [52]) was injected into the prepared holes using a cartridge system, followed by the insertion of the steel anchors. For the lead-bonded samples, pure lead was heated to approximately 800 °C until molten and then poured into the holes to embed the anchors, forming a metallic bond upon solidification. After installation, all specimens were left undisturbed for seven days to allow sufficient curing and development of bond strength.

The pull-out tests were performed in accordance with ASTM D4435-13e1 [44] using a portable hydraulic system. The setup included a hydraulic jack with a maximum capacity of 750 kN, a pressure gauge for monitoring applied loads, and specially designed steel grips to secure the anchors. A rigid conical head was employed to minimize eccentric loading effects and secondary stresses. Each specimen was subjected to monotonically increasing axial tensile load until failure, while load-displacement responses were recorded (Table 7).

The applied forces were calculated based on the measured hydraulic pressure and piston geometry. Multiple loading cycles were conducted to evaluate both the ultimate capacity and the post-peak response. While elastic deformations were partially recovered after unloading, residual plastic deformations were observed in the surrounding material.

The applied tensile load was computed based on the following relationship [15]:

$$F_{push} = p\left(\frac{\pi {D_b}^2}{4}\right) \quad (1)$$

where F_{push}denotes the applied tensile force, p represents the gauge pressure (converted from bar to N/mm²), and $D_b$is the piston bore diameter.

Table 7. Axial pull-out test results of equivalent anchors obtained 21 days after installation [15]

No	Test Code	Anchor Diameter (mm)	Embedment Depth (mm)	Bore Diameter (mm)	Maximum Displacement (mm)	Maximum Pressure (bar)	Maximum Pull-Out Force (kN)
1	PL-1	16	200	98	45	8.00	0.61
2	PL-2	16	200	98	48	10.00	0.76
3	PL-3	16	200	98	50	6.00	0.46
4	PE-1	16	200	98	50	58.00	4.45
5	PE-2	16	200	98	47	53.00	4.07
6	PE-3	16	200	98	46	60.00	4.61

In addition to the tabulated results, the load-displacement (slip) response obtained from the pull-out tests is presented in Fig. 12, providing a clear comparison of the anchorage performance of the two bonding systems. A marked difference was observed between the lead-bonded clamps (PL series) and epoxy-bonded clamps (PE series). The PL specimens exhibited relatively low pull-out capacities, ranging from 0.46 to 0.76 kN, with corresponding pressure levels limited to 6-10 bar. Their load–displacement curves were characterized by low peak resistance followed by a relatively abrupt post-peak reduction, indicating early debonding, limited mechanical interlock, and a brittle response with minimal residual load-carrying capacity. This reduced performance can be attributed to the practical difficulties associated with the use of molten lead, particularly in inclined arch geometries, where rapid solidification may prevent complete filling of the boreholes and reduce bonding efficiency under axial tensile loading. In contrast, the PE specimens demonstrated substantially higher tensile capacities, varying between 4.07 and 4.61 kN, with an average value of 4.38 kN, corresponding to approximately seven times the capacity of the lead-bonded specimens. The epoxy-bonded clamps also exhibited much higher pressure levels, ranging from 53 to 60 bar, and a steeper initial stiffness in the load-displacement response. After reaching the peak load, the PE specimens showed a gradual post-peak softening behavior, suggesting progressive bond degradation and frictional slip development along the anchor–stone interface. Although both bonding systems reached similar displacement levels at failure, approximately 45-50 mm, the superior performance of epoxy was mainly associated with its enhanced bonding efficiency and more stable post-peak response rather than increased deformability.

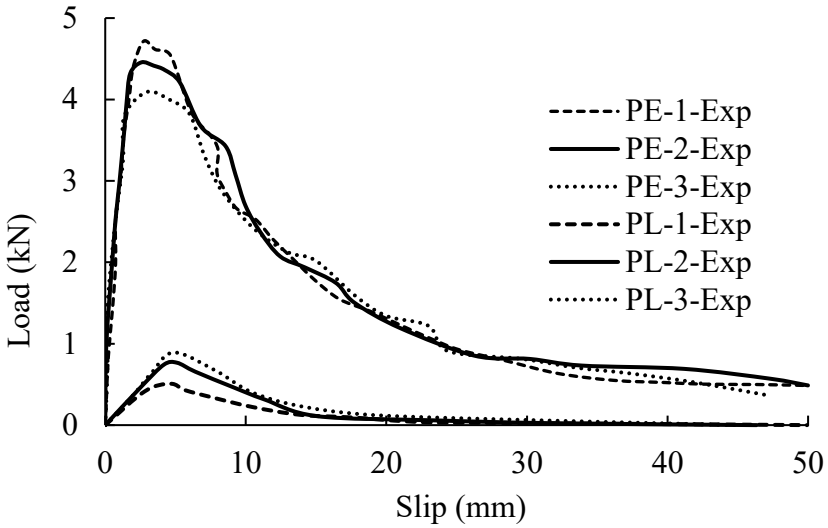


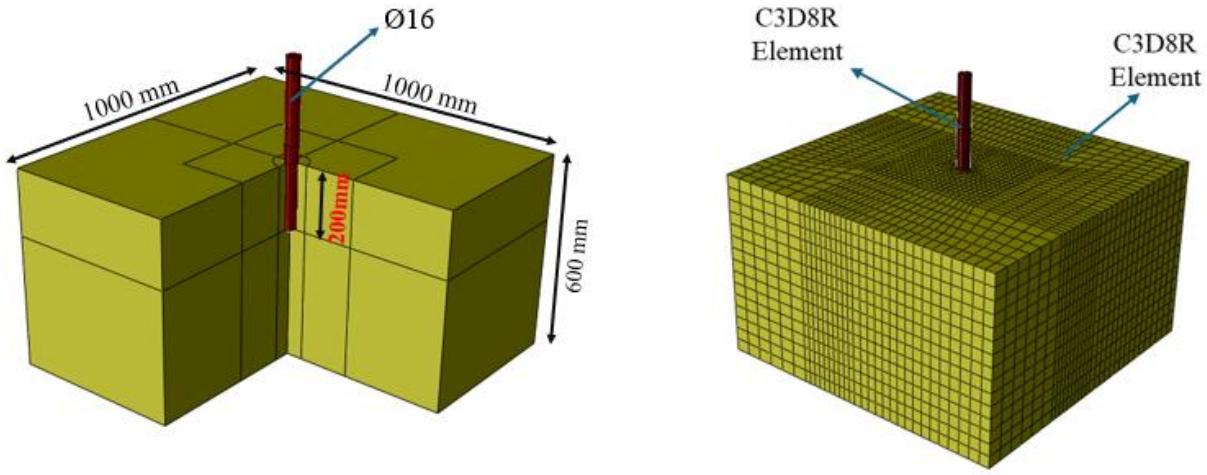
Figure 12. Load–displacement (slip) curves of epoxy and lead-bonded anchors obtained from pull-out tests

Overall, the experimental findings confirm that epoxy-based clamp systems provide a more reliable and effective solution for the strengthening of historical stone arch structures. Its high adhesion capacity and favorable application characteristics make epoxy a preferable alternative to traditional lead-based bonding methods.

5. Numerical Modeling and Strengthening Analysis

5.1. Finite Element Model Verification of Anchor Pull-Out Test

In the experimental study, both lead and epoxy were used as bonding materials, and it was observed that epoxy exhibited significantly higher bond strength, as presented in Table 7. Since the epoxy-bonded specimens exhibited substantially higher pull-out capacity and more reliable anchorage performance than the lead-bonded specimens, the cohesive interface parameters used in the subsequent numerical arch models were calibrated based on the epoxy-bonded pull-out response. A comparable experimental-numerical strategy has recently been adopted in interface studies for strengthening systems, where pull-out test results were used to characterize local bond-slip behavior and to calibrate cohesive interaction laws for finite element simulations [47]. Therefore, a finite element calibration study was conducted to accurately define the material parameters to be used in numerical modeling, particularly for the anchorage interface behavior. In this context, a detailed finite element model replicating the experimental pull-out test setup was developed in Abaqus, as illustrated in Fig. 13.



(a) (b)

Figure 13. (a) Geometry of the finite element model, (b) Mesh discretization of the model.

The finite element model was developed to represent the experimental setup, incorporating a 16 mm diameter 304 stainless steel anchor embedded in the stone block with a depth of 200 mm. The mechanical properties of the anchor material were defined based on the data provided in Table 6. The anchor was subjected to monotonic axial tensile loading to simulate the pull-out behavior. The interaction between the anchor and the surrounding material was modeled using a surface-based cohesive contact formulation based on the traction–separation law available in Abaqus, as shown in Fig. 14.

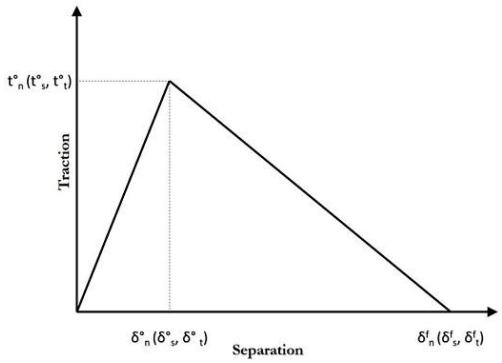


Figure 14. Traction separation law available in ABAQUS [48]

In this approach, the interface behavior is governed by a linear elastic traction-separation relationship prior to damage initiation, which can be expressed as:

$$\begin{bmatrix} t_n \\ t_s \\ t_t \end{bmatrix} = \begin{bmatrix} K_{nn} & 0 & 0 \\ 0 & K_{ss} & 0 \\ 0 & 0 & K_{tt} \end{bmatrix} \begin{bmatrix} \delta_n \\ \delta_s \\ \delta_t \end{bmatrix} \quad (2)$$

where t_n, t_s, t_trepresent the normal and shear tractions, $\delta_n, \delta_s, \delta_t$denote the corresponding separations, and $K_{nn}, K_{ss}, K_{tt}$are the stiffness coefficients defining the initial elastic response of the interface. Damage initiation was defined using the quadratic nominal stress criterion (QUADS), expressed as:

$$\left(\frac{t_n}{t_{n0}}\right)^2 + \left(\frac{t_s}{t_{s0}}\right)^2 + \left(\frac{t_t}{t_{t0}}\right)^2 = 1 \quad (3)$$

where $t_{n0}, t_{s0}, t_{t0}$are the peak nominal stresses in normal and shear directions. In this study, the damage initiation stresses were defined as $t_n = 1.0 \times 10^6$Pa and $t_s = t_t = 1.7 \times 10^5$Pa, calibrated to match the experimentally observed pull-out capacity.

Following damage initiation, the degradation of the interface stiffness was governed by a displacement-based damage evolution law, where the damage variable evolves as a function of effective displacement. The characteristic displacement at complete failure was defined as $\delta_f = 0.002$, allowing the model to capture the post-peak softening behavior observed in the experiments. In addition, the cohesive stiffness parameters were defined as $K_{nn} = K_{ss} = K_{tt} = 6.0 \times 10^7$Pa/m, ensuring a realistic representation of the initial stiffness without introducing excessive numerical stiffness. A frictional behavior was also incorporated with a friction coefficient of 0.02 and a maximum shear traction limit ($\tau_{max} = 1.7 \times 10^5$ Pa), enabling the simulation of residual load-carrying capacity after bond failure.

All cohesive parameters were calibrated iteratively to reproduce an ultimate pull-out load of approximately 5 kN, consistent with the experimental results. The adopted traction-separation framework successfully captured both the peak load and the post-peak softening behavior, providing a reliable representation of the bond–slip mechanism between the anchor and the surrounding material. The load–displacement response obtained from the finite element analysis was compared with the experimental results, as presented in Fig. 15. It was observed that the numerical predictions are in close agreement with the experimental data, with an approximate error of about 5% in terms of peak load and overall response. In addition, the initial stiffness and the gradual post-peak degradation observed in the experiments were accurately reproduced by the numerical model.

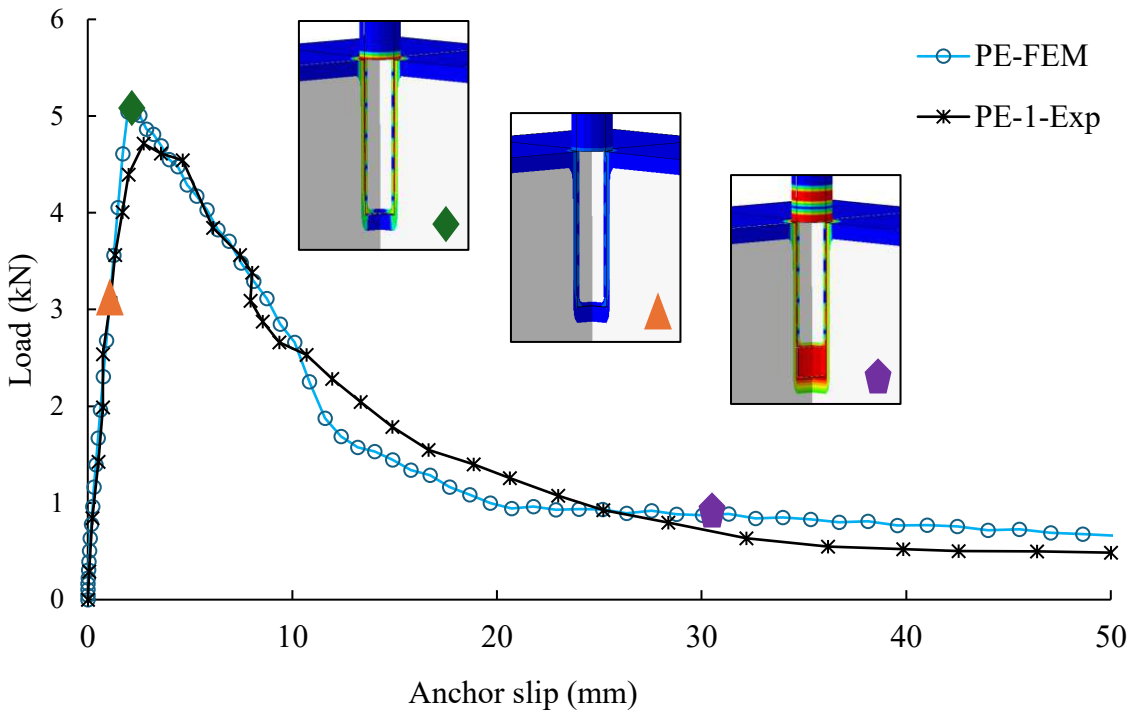


Figure 15. Comparison of load-displacement responses from finite element analysis and experimental pull-out test.

To further validate the modeling approach, the stress distribution and deformation patterns obtained from the finite element analysis were examined at different stages of loading. As illustrated in Fig. 16, the maximum principal stress contours indicate that stress concentrations initially develop around the anchor interface region and progressively propagate along the embedment depth as the applied load increases. This behavior is consistent with the experimentally observed bond failure mechanism, where damage initiates near the loaded end and extends downward during pull-out. Moreover, the vertical displacement contours (U2) clearly demonstrate the progressive slip of the anchor, confirming the development of bond–slip behavior along the interface.

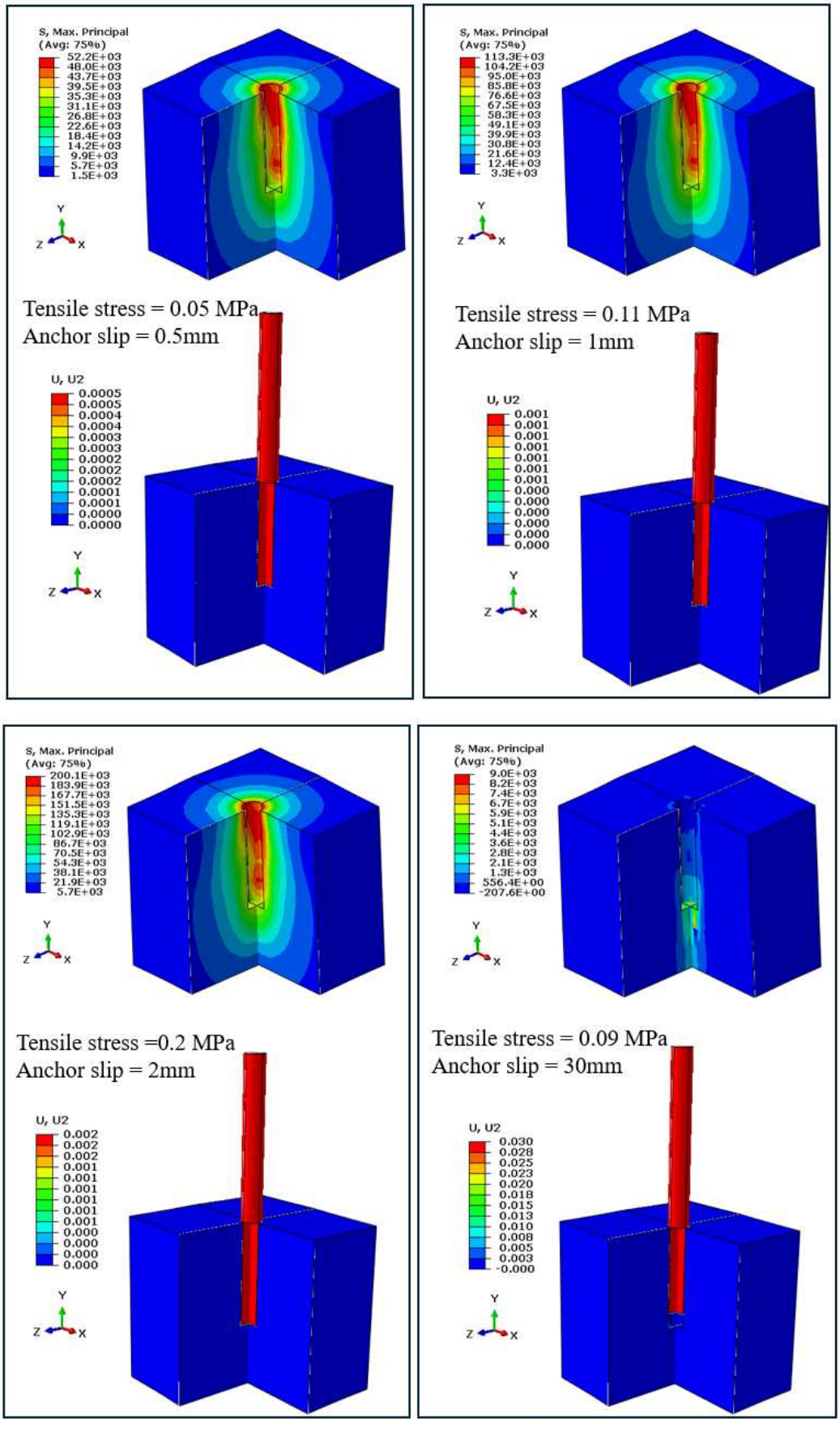


Figure 16. Evolution of stress distribution and interface slip during the anchor pull-out process

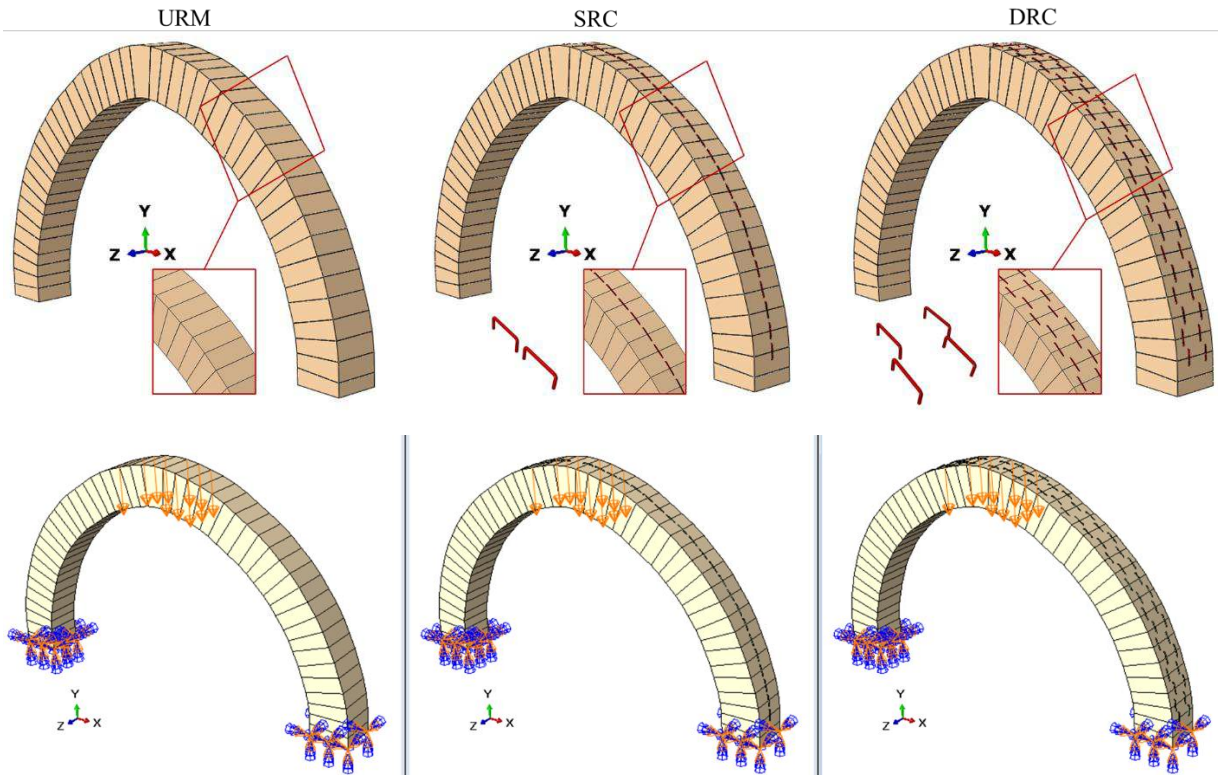
At higher displacement levels, a significant reduction in stress transfer is observed, indicating the degradation of bond capacity and the transition to a residual frictional resistance mechanism. This is also reflected in the load-displacement curve, where the post-peak softening corresponds to the progressive loss of cohesive interaction. The consistency between the stress contours, displacement fields, and global load-displacement response provides strong evidence that the numerical model accurately captures both the local failure mechanisms and the global structural behavior.

Based on these observations, it can be concluded that the adopted cohesive modeling approach provides a robust and physically consistent representation of bond behavior. Therefore, the validated modeling strategy was subsequently employed in the micro-modelling of clamp-reinforced arch systems, enabling a more reliable assessment of structural performance under different strengthening configurations. This validation significantly enhances the reliability and credibility of the numerical results obtained in the subsequent analyses.

5.2. Micro-Modeling of the Arch System

Following the validation of the cohesive interface model through the anchor pull-out test, the proposed modeling strategy was extended to the micro-modelling of a masonry arch system in order to investigate the structural response and the effectiveness of clamp-based strengthening configurations. The three-dimensional finite element models of the arch were developed in Abaqus, as illustrated in Fig. 17. The arch geometry consists of a span of 9.3 m and a rise of 7.4 m, and is composed of 47 stone blocks, each with approximate dimensions of 1.0 m × 0.8 m × 0.36 m.

Three different configurations were considered, as shown in Fig. 15: (i) the unreinforced model (URM), representing the arch without clamps, (ii) the single-row clamp model (SRC), and (iii) the double-row clamp model (DRC). In the strengthened configurations (SRC and DRC), all stone blocks were interconnected using steel clamps arranged along the arch profile in either single or double rows. All models were constructed using solid elements (C3D8R), and a mesh sensitivity analysis was conducted to ensure solution accuracy. Based on this analysis, a mesh size of 0.1 m was adopted for the stone blocks, while a finer mesh size of 0.01 m was used for the clamps to better capture local stress concentrations.

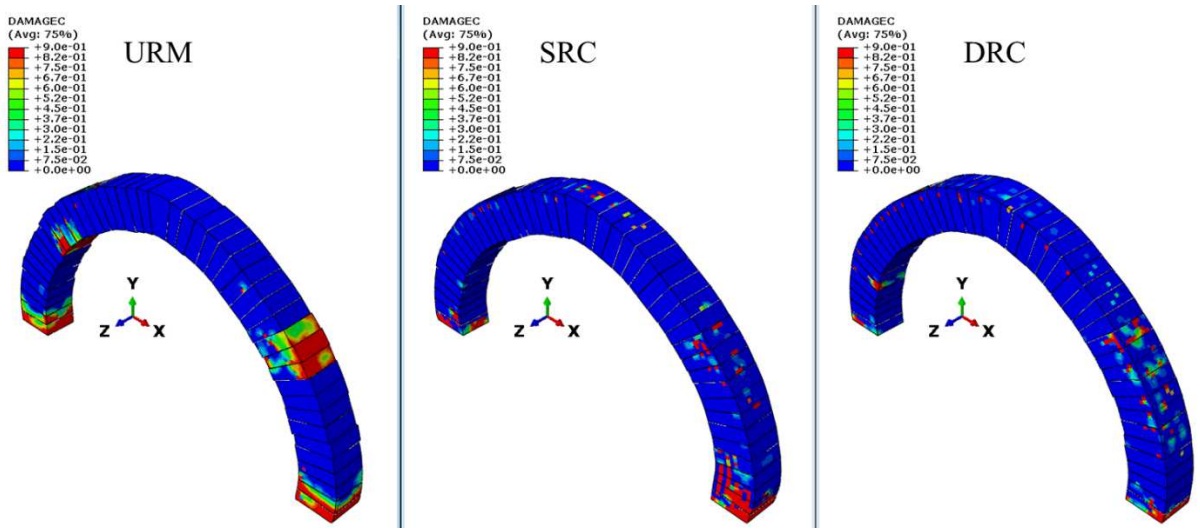


(a) (b) (c)

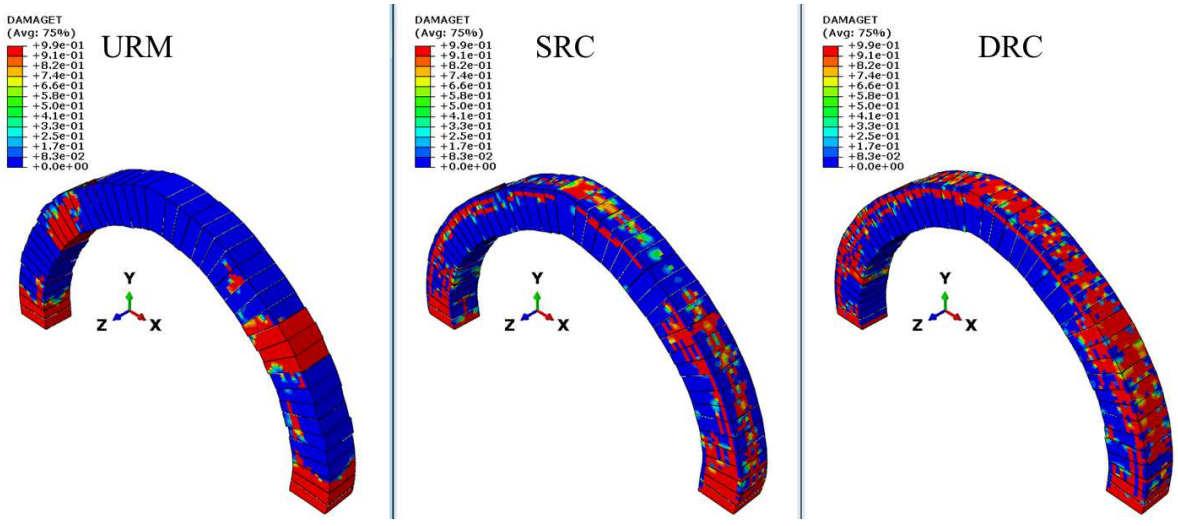
Figure 17. Three-dimensional finite element micro-models of the arch stones: (a) non-strengthened (without clamps), (b) single-row clamped, and (c) double-row clamped configurations.

The mechanical properties of the stone material were defined based on the values presented in Table 3, and damage behavior was included in the material model. The clamps were modeled using structural steel (S420), and both elastic and plastic behavior were considered in order to realistically represent yielding under loading conditions. Contact interactions between stone blocks were defined using a frictional contact formulation combined with a cohesive behavior to represent the mortar-like interaction between adjacent stones. For the clamp–stone interfaces, the cohesive parameters calibrated in the pull-out verification study were directly adopted. Boundary conditions were defined by fixing the supports at the base of the arch, which is considered appropriate for representing a rigid foundation condition. The structural response of the arch system was investigated through both static and dynamic analyses. In the static analysis, a displacement-controlled loading scheme was adopted, in which a vertical displacement of up to 300 mm was applied at the crown of the arch to evaluate its load–deformation behavior. In addition, dynamic analyses were performed to evaluate the seismic response of the arch system. In this regard, acceleration time histories were applied

simultaneously in three orthogonal directions, with the input motions scaled to a peak ground acceleration (PGA) of 0.2g. All analyses were conducted using a two-step procedure. In the first step, a Static General analysis was performed to apply gravity loading and allow the structure to reach equilibrium under its self-weight. In the second step, different analysis approaches were adopted depending on the loading condition. For the static case, displacement-controlled loading was applied at the crown of the arch. For the dynamic case, a Dynamic Implicit analysis procedure was employed, in which seismic acceleration records were imposed on the model. Geometric nonlinearity (NLGEOM) was considered in all analyses to accurately capture large deformations and nonlinear structural response.



(a)



(b)

Figure 18. Damage distribution due to (a) compressive and (b) tensile stresses

The dynamic analysis results clearly demonstrate the significant influence of clamp application on the structural behavior of the arch system. In the unreinforced model, both compressive and tensile damage are highly localized, with damage variables (DAMAGET and DAMAGEC) approaching values close to 0.9-1.0 in critical regions, indicating severe stress concentrations and the formation of unstable failure mechanisms. In contrast, the clamped configurations exhibit a more distributed damage pattern, with damage values generally spread over a wider region but remaining at comparatively lower intensities, suggesting improved load redistribution and enhanced structural integrity (Fig. 18).

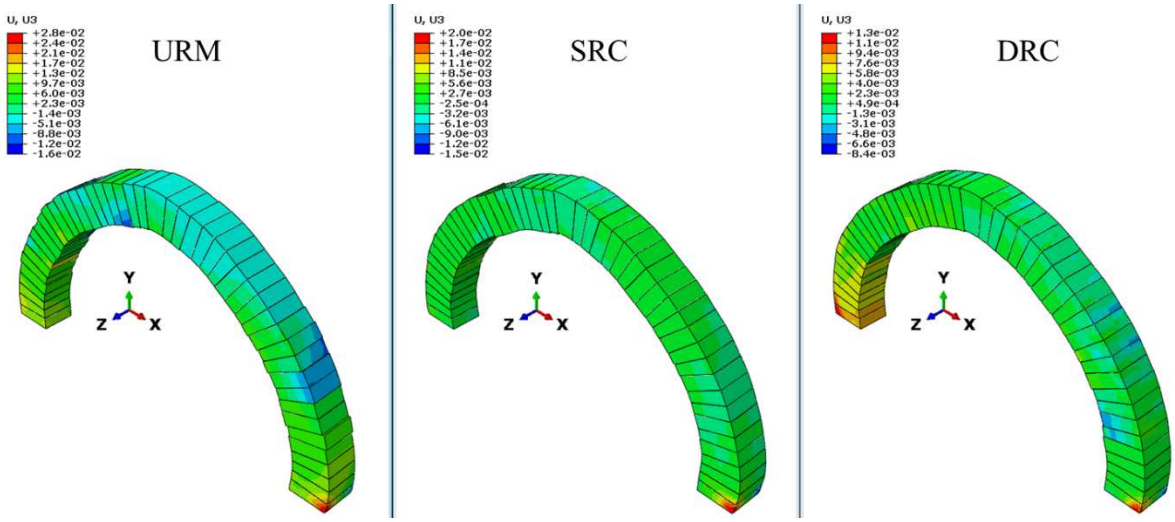


Figure 19. Out-of-plane displacements (mm)

In particular, the double-clamp configuration shows the most favorable behavior, with a noticeable reduction in out-of-plane displacements and a more uniform stress distribution along the arch. The maximum out-of-plane displacement (U3) in the unreinforced model reaches approximately 28 mm, whereas this value decreases to about 15 mm in the single-clamp model and further reduces to approximately 12 mm in the double-clamp configuration (Fig. 19). Similarly, while peak tensile damage values remain high locally in the unreinforced case, the clamped models exhibit a more homogeneous distribution, with fewer regions reaching critical damage levels.

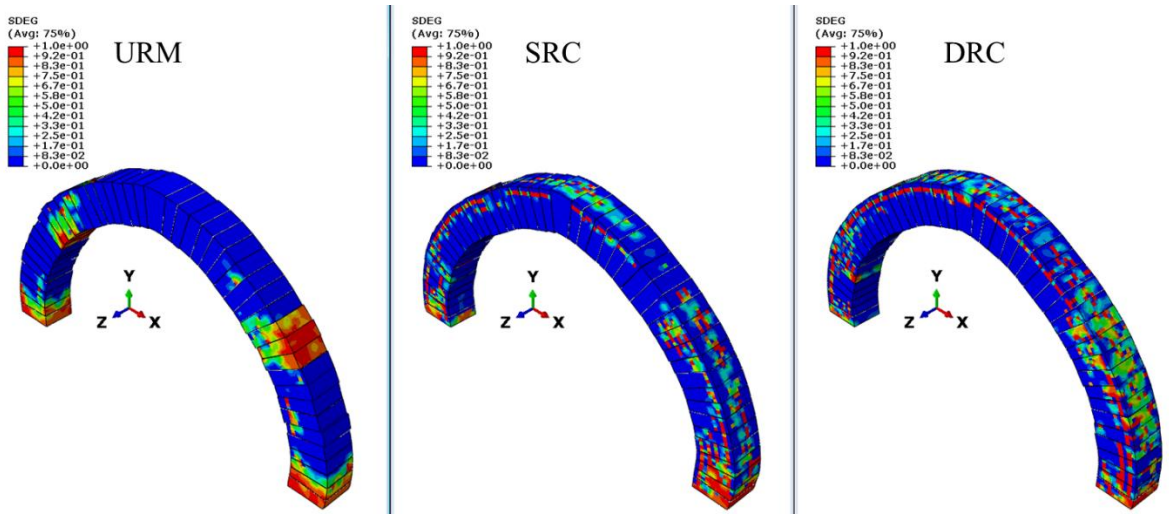


Figure 20. Damage distribution after the analysis

Although the overall damage region appears more widespread in the clamped configurations, the intensity of damage is lower and more evenly distributed, indicating that a larger portion of the structure participates in load transfer (Fig. 20). This behavior confirms that the clamps enhance structural continuity, suppress local instabilities, and significantly improve the dynamic performance of the system. Following the dynamic analyses, static analyses were conducted to further evaluate the fundamental load-deformation characteristics of the arch system and to provide a clearer interpretation of the influence of clamp configurations under controlled loading conditions.

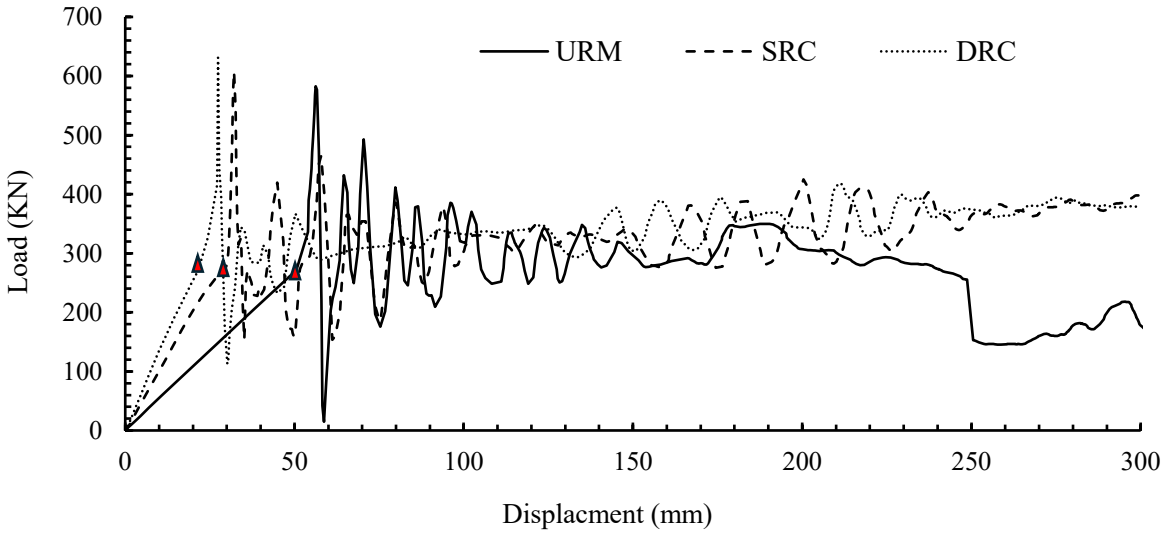


Figure 21. Load–displacement curves of URM, SRC, and DRC configurations under static loading

The static analysis results indicate a distinct variation in structural response among the three configurations (URM, SRC, and DRC). In the unreinforced model (URM), both deformation

and damage are highly localized, particularly near critical regions such as the crown and supports. This localized behavior leads to abrupt changes in the load-displacement response and indicates the development of unstable failure mechanisms. In contrast, the clamped configurations (SRC and DRC) exhibit a more distributed deformation pattern. The presence of clamps enhances the interaction between adjacent stone blocks, allowing the structure to behave more integrally. As a result, deformation is no longer concentrated in limited regions but is instead spread along a larger portion of the arch.

A comparison of the load–displacement responses in the initial (elastic) range further highlights the effect of clamp application (Fig. 21). At comparable load levels, the displacement of the single-clamp configuration (SRC) is reduced by approximately 35% relative to the unreinforced model (URM), while the double-clamp configuration (DRC) achieves a reduction of about 45%. In addition, the transition from SRC to DRC provides an additional improvement of approximately 15%, indicating a clear increase in the initial stiffness of the system with increasing clamp density. The load–displacement curves further support these observations. Although the URM configuration attains a relatively higher peak load, this is followed by a rapid loss of load-carrying capacity, indicating a brittle response. The SRC model demonstrates more controlled behavior, with reduced fluctuations and improved load sustainability. The DRC configuration provides the most stable response, maintaining a consistent load level over a wider displacement range and exhibiting the least pronounced oscillations (Fig. 22).

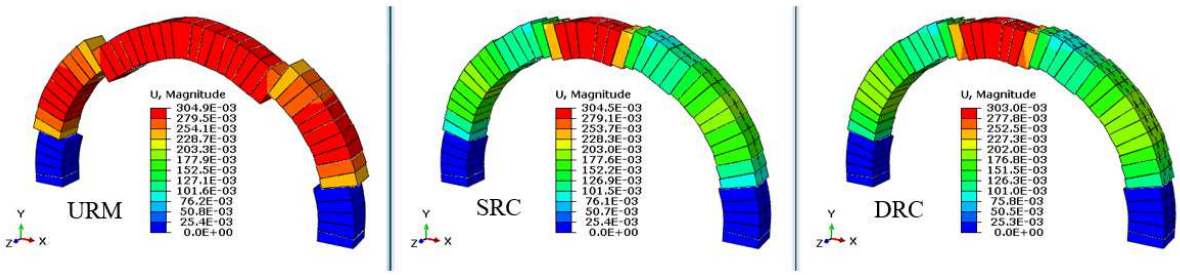


Figure 22. Comparison of displacement distributions for URM, SRC, and DRC models under static loading

As shown in Fig. 23, the distribution of tensile damage is also consistent with the general trend. In the URM model, cracking is concentrated within limited zones, whereas in the SRC and especially the DRC configurations, damage spreads over a wider region with reduced intensity. This indicates that a larger number of stone blocks participate in resisting the applied load, resulting in improved load redistribution and enhanced structural stability. Overall, the static

analysis results confirm that the application of clamps significantly improves the structural response by reducing localization effects, enhancing load transfer continuity, and promoting more stable and ductile behavior.

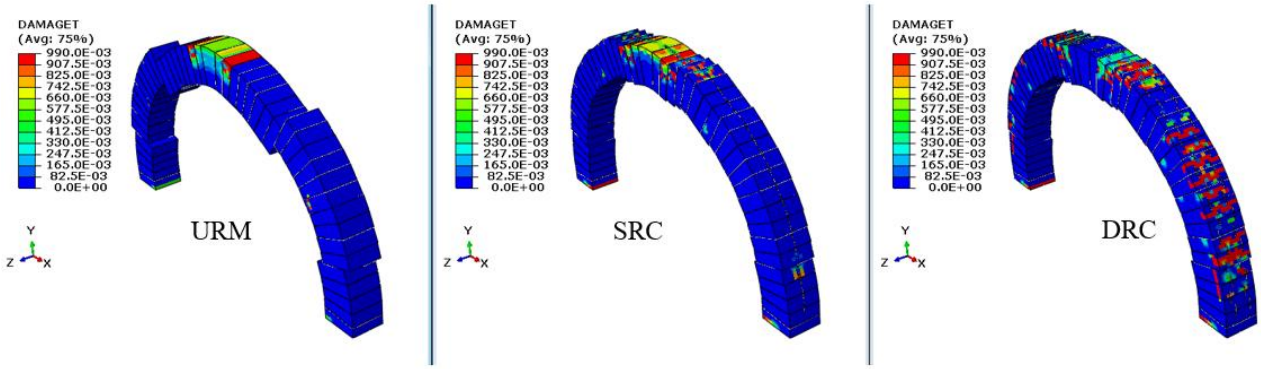


Figure 23. Tensile damage (DAMAGET) contours of URM, SRC, and DRC configurations under static analysis

5.3 Numerical Modeling of the Harran Ulu Mosque Entrance Arches

In order to represent the real structural condition of the Harran Ulu Mosque entrance arches, three different finite element models were developed within the scope of this study (Fig. 24). In the first model, the existing condition of the structure was represented by assigning the mechanical properties of the masonry units based on a compressive strength of 2.5 MPa. This model reflects the current state of the arch system without any strengthening intervention.

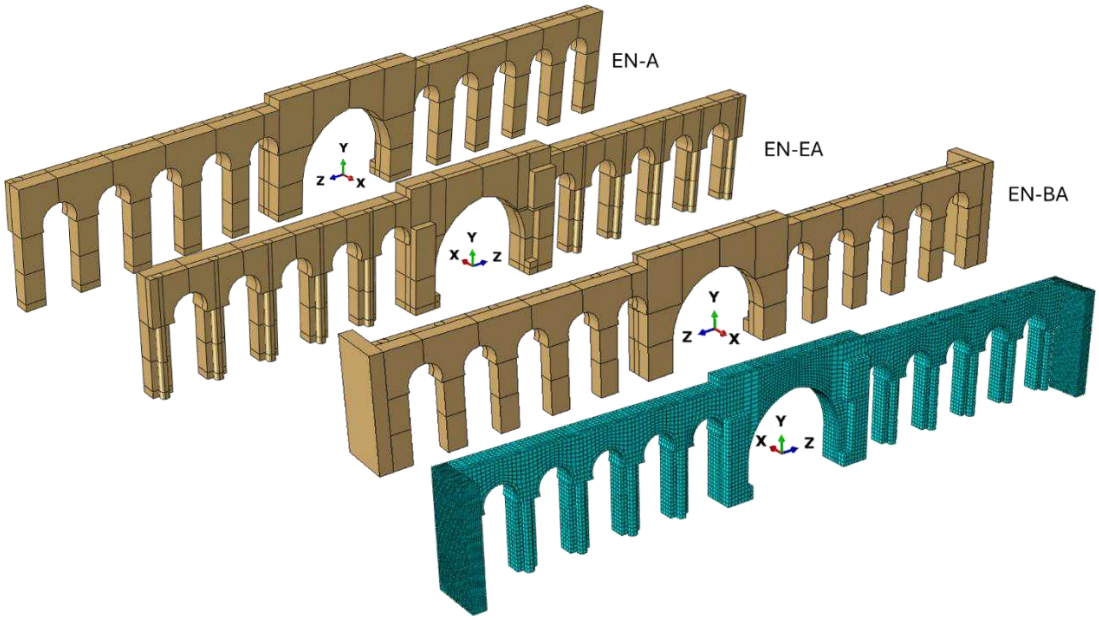


Figure 24. Three-dimensional finite element models of the Harran Ulu Mosque entrance arches: (EN-A) existing condition, (EN-EA) enhanced, and (EN-BA) buttressed configurations

In the second model, the effect of clamp-based strengthening was incorporated by considering the improvement observed in the previously conducted single- and double-clamp analyses. Based on these results, an improvement ratio of approximately 30% was adopted. Accordingly, the mechanical properties of the masonry units were enhanced, and an increased compressive strength of 3.25 MPa was assigned to represent the improved interaction between stone blocks due to clamp application. Thus, the clamp-enhanced entrance arch model represents the structural improvement associated with the epoxy-bonded mechanical steel stitching system. In the third model, in addition to the material improvement, a structural intervention was introduced to address out-of-plane instability mechanisms under dynamic loading conditions such as earthquakes. In this context, buttress-like lateral support walls were modeled at the ends of the arch in order to restrain out-of-plane displacements and prevent overturning mechanisms. The effectiveness of this intervention in improving the global stability of the arch system was investigated through numerical analyses. Thus, three distinct arch configurations were considered: (i) the entrance arch model (EN-A), representing the existing condition, (ii) the enhanced entrance arch model (EN-EA), reflecting improved inter-block behavior due to clamp application, and (iii) the buttressed entrance arch model (EN-BA), incorporating additional lateral restraint against out-of-plane failure.

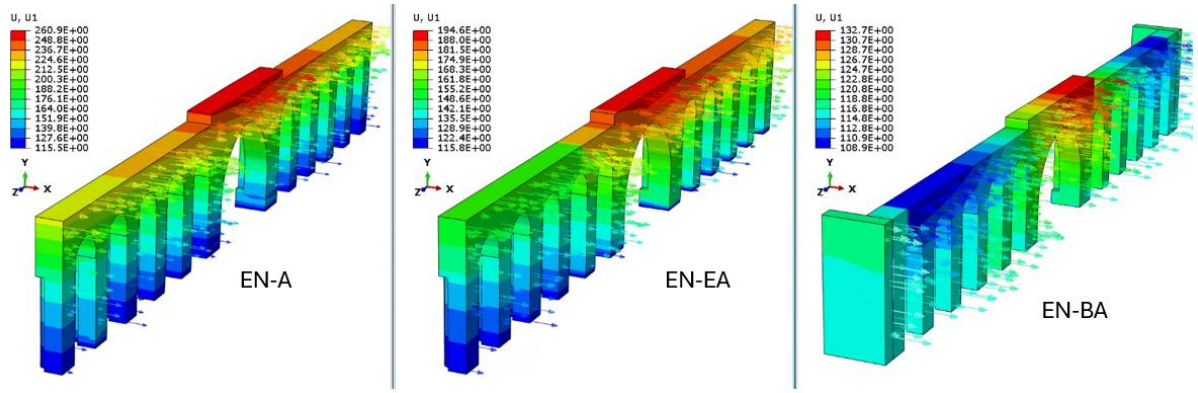
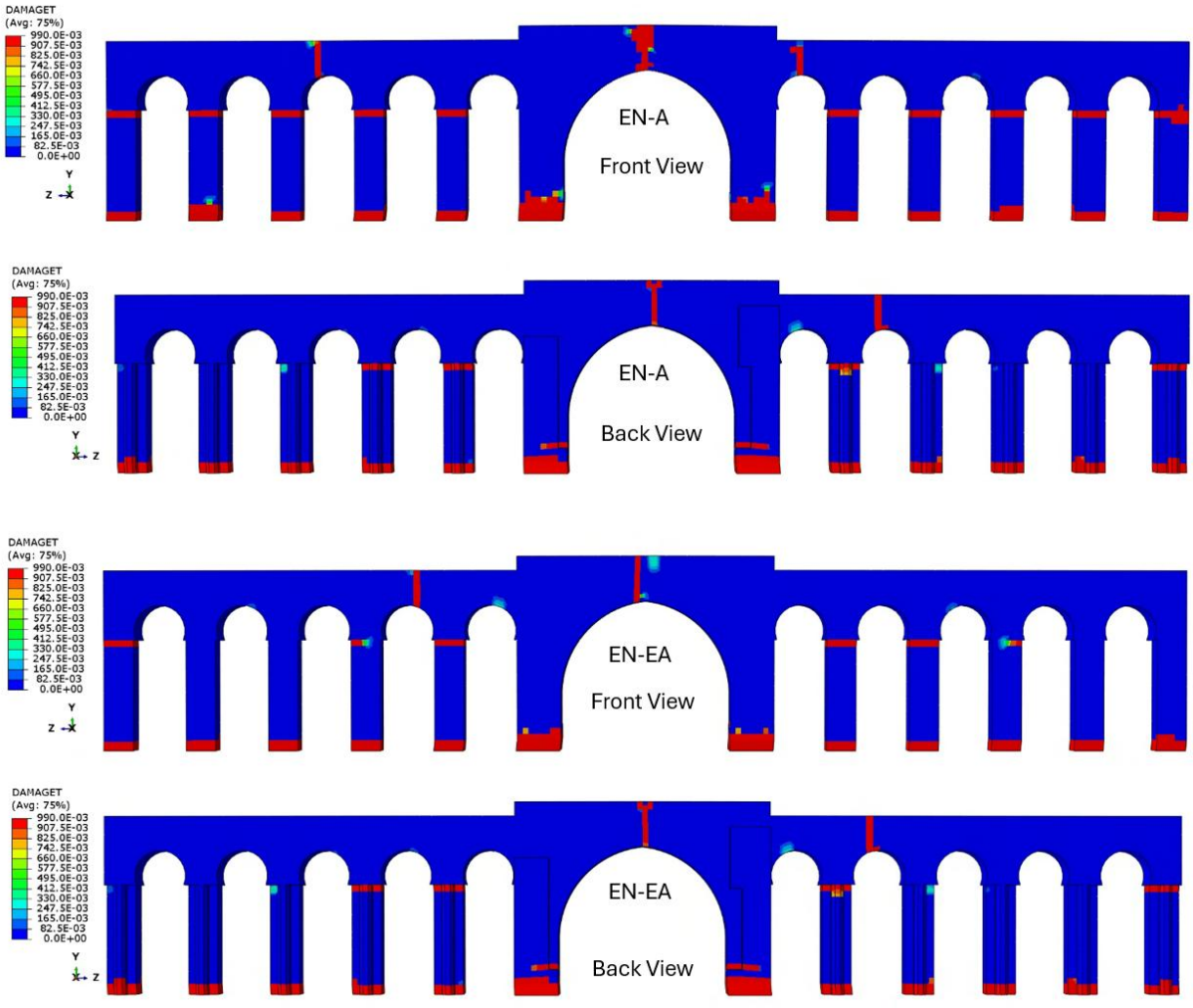


Figure 25. Comparison of out-of-plane displacements (U1) for EN-A, EN-EA, and EN-BA models

As shown in Fig. 25, the dynamic analysis results provide a clear comparison of the structural response of the three configurations, namely EN-A, EN-EA, and EN-BA, in terms of damage evolution and out-of-plane displacements (U1). The U1 displacement contours, representing out-of-plane deformation, reveal a significant reduction in displacement levels with the application of strengthening measures. In the EN-A model (existing condition), the maximum

out-of-plane displacement reaches approximately 260 mm, indicating a highly flexible response and pronounced instability under dynamic excitation. This level of deformation suggests a strong tendency toward out-of-plane failure mechanisms.

In contrast, the EN-EA model (enhanced material due to clamp effect) exhibits a noticeable reduction in maximum displacement, with peak values decreasing to approximately 195 mm. This corresponds to an approximate 25% reduction in out-of-plane displacement compared to the EN-A model. The improved material properties enhance inter-block interaction, leading to a stiffer and more coherent structural response. The EN-BA model (buttressed configuration) demonstrates the most significant improvement. The maximum out-of-plane displacement is further reduced to approximately 130-135 mm, representing nearly a 50% reduction relative to the EN-A model and about a 30-35% reduction compared to the EN-EA model. This clearly indicates that the addition of buttress-like lateral supports is highly effective in restraining out-of-plane movements and suppressing overturning mechanisms.



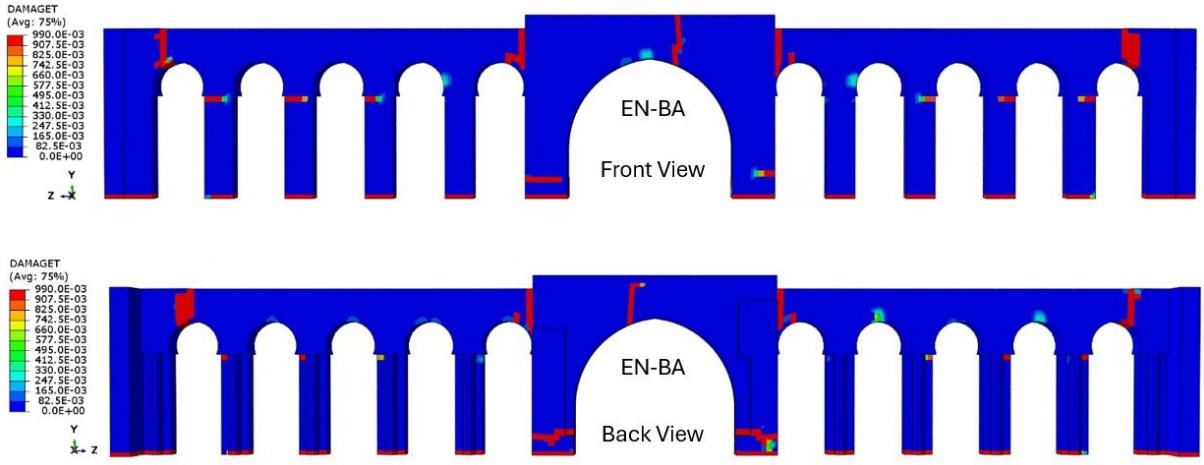


Figure 26. Tensile damage (DAMAGET) contours of EN-A, EN-EA, and EN-BA configurations under seismic loading

The damage distributions (DAMAGET) further support these findings. In the EN-A model, tensile damage is highly localized, particularly at the arch crown and support regions, indicating the formation of critical failure zones and the initiation of unstable cracking mechanisms (see Fig. 26). In the EN-EA configuration, although damage is still present, it becomes more distributed along the arch, reflecting improved interaction between adjacent blocks and a more effective load transfer mechanism.

In the EN-BA model, the intensity of tensile damage is noticeably reduced and more uniformly distributed across the structure. This indicates that the arch behaves as a more integrated system, with a larger number of masonry units contributing to load resistance. The reduction in localized damage concentrations suggests a delay in crack initiation and propagation, which is directly associated with enhanced global stability.

Overall, the DAMAGET results clearly demonstrate that while material-level improvement (EN-EA) leads to a more distributed damage pattern, the introduction of structural restraints in the EN-BA configuration provides a more significant reduction in damage intensity and localization. This highlights the effectiveness of buttress-type interventions in controlling crack development and improving the overall seismic performance of masonry arch systems.

6. Construction Stages of the Harran Ulu Mosque Entrance

The entrance arches of the Harran Ulu Mosque were originally constructed in the 8th century (700s) and have undergone several restoration phases throughout their history. Due to various natural and human-induced events, particularly the Mongol invasions, the structure suffered significant damage over time. In the modern period, the first major restoration was carried out in 2015. During this intervention, only the central arch remained standing, while the surrounding arches had completely collapsed, as illustrated in Fig. 27. Within the scope of this restoration, four additional arches were reconstructed symmetrically, resulting in a five-arch configuration.

Subsequently, the structure was exposed to the 6 February 2023 Kahramanmaraş earthquakes, which caused further damage to the arch system. As shown in Fig. 27, the outermost two arches constructed during the 2015 restoration collapsed entirely, while the adjacent arches experienced partial damage [49]. Post-earthquake assessments revealed varying levels of structural degradation, necessitating a new restoration intervention.



Figure 27. Chronological development and seismic damage of the Harran Ulu Mosque arches

Following the earthquake, a comprehensive restoration program was implemented. Severely damaged arches were dismantled, while moderately damaged ones were carefully disassembled under controlled conditions and reconstructed. As part of this process, the arch system was expanded and redesigned to consist of a total of eleven arches, arranged symmetrically with five arches on each side of the central arch.



Figure 28. Post-earthquake reconstruction stages of the Harran Ulu Mosque arches

The reconstruction process involved several stages, as documented in Fig. 28. Initially, the vertical supporting elements (columns) were constructed. To ensure adequate transverse connectivity and structural integrity, horizontal interlocking connections (clamps) were introduced between the masonry units at the column level. As the construction progressed upward, double-clamp systems, whose effectiveness was previously demonstrated through numerical analyses, were implemented particularly in the arch regions to enhance inter-block interaction and overall stability. The step-by-step construction process and application of these strengthening techniques are illustrated in Fig. 28.



Figure 29. Final condition of the Harran Ulu Mosque entrance arches after restoration

As illustrated in Fig. 29, following the completion of the restoration works, the necessary structural interventions were carried out, and the historic structure was carefully reopened to visitors in a safe and stable condition, ensuring both its preservation and continued use.

7. Conclusion

This study investigated the effectiveness of epoxy-bonded mechanical steel stitching as a strengthening technique aimed at improving the structural integrity of historical stone masonry arches while maintaining compatibility with the original masonry fabric. The research combined material characterization, in-situ pull-out tests, finite element calibration, three-dimensional arch micro-modeling, and a case-study application on the entrance arches of the Harran Ulu Mosque, which were damaged during the 2023 Kahramanmaraş earthquakes. Based on the experimental and numerical results, the following conclusions can be drawn:

- The pull-out tests clearly demonstrated that the embedment material plays a decisive role in the anchorage performance of mechanical steel stitches. Lead-bonded clamps exhibited relatively low pull-out capacities ranging from 0.46 to 0.76 kN, whereas epoxy-bonded clamps reached values between 4.07 and 4.61 kN, with an average capacity of 4.38 kN. This corresponds to approximately seven times higher pull-out resistance compared with lead-bonded specimens. Therefore, epoxy provided a more reliable bond mechanism and was selected as the basis for the subsequent numerical interface calibration.
- The finite element model of the pull-out test, developed using a cohesive contact formulation, reproduced the experimental load-displacement response with an error of approximately 5% in terms of peak load. The calibrated interface parameters successfully represented the bond–slip behavior between the steel connector and the surrounding stone material. This provided a reliable basis for implementing the clamp-stone interaction in the numerical arch models.
- The three-dimensional arch models demonstrated that mechanical clamps significantly improve the structural response of stone masonry arches. In the unreinforced model, tensile and compressive damage were concentrated in limited critical regions, indicating the development of unstable local failure mechanisms. In contrast, the single-row and double-row clamp configurations distributed damage over a wider region with lower intensity, showing improved load redistribution and enhanced inter-block continuity.

- The dynamic analyses showed that clamp application substantially reduced out-of-plane displacement demand. The maximum absolute out-of-plane displacement decreased from approximately 28 mm in the unreinforced model to 15 mm in the single-row clamp model and to 12 mm in the double-row clamp model. This result indicates that increasing clamp density improves lateral stability and reduces the risk of out-of-plane failure.
- Static analyses further confirmed the beneficial effect of clamp-based strengthening. The single-row clamp configuration reduced displacement demand by approximately 35% relative to the unreinforced model, while the double-row clamp configuration achieved a reduction of approximately 45%. The double-row clamp model also exhibited the most stable load-displacement response, with reduced fluctuations and improved post-peak behavior.
- In the case-study analysis of the Harran Ulu Mosque entrance arches, the existing condition model exhibited a maximum out-of-plane displacement of approximately 260 mm, indicating a pronounced tendency toward out-of-plane instability. The clamp-enhanced model reduced this value to approximately 195 mm, corresponding to a reduction of about 25%. When buttress-like lateral restraints were introduced, the maximum displacement further decreased to approximately 135 mm, representing nearly a 50% reduction compared with the existing condition.
- The tensile damage distributions obtained from the case-study models showed that clamp-based strengthening improved inter-block interaction and reduced localized damage concentration. However, the addition of lateral restraint provided a more pronounced improvement in global stability, particularly against out-of-plane deformation and overturning mechanisms.

Overall, the results confirm that epoxy-bonded mechanical steel stitching is an effective and heritage-compatible strengthening strategy for historical stone masonry arches. Among the investigated configurations, the double-row clamp arrangement provided the most favorable performance in terms of displacement reduction, damage redistribution, and structural stability. The findings also indicate that clamp-based strengthening can be further enhanced when combined with appropriate lateral restraint systems, particularly in arch systems vulnerable to out-of-plane seismic response. Future studies should include full-scale experimental testing of clamp-strengthened stone arches and long-term durability assessments of epoxy-bonded steel connectors under environmental exposure conditions.

Acknowledgment

The authors would like to thank Gaziantep Directorate of Surveying and Monuments, Anıt Restorasyon and Dynamica Mühendislik Co for their valuable supports.

Author contributions: All authors contributed equally to the conception, investigation, analysis, and writing of this study. Each author participated actively in all phases of the research and jointly approved the final manuscript.

Funding

This research received no external funding.

Data Availability

No data was used for the research described in this article.

Declarations

Competing Interests: The authors declare that they have no known competing financial interests or personal relationships that could have appeared to influence the work reported in this paper.

Declaration of AI and AI-assisted technologies in the writing process During the preparation of this manuscript, the authors used ChatGPT, an AI language model developed by OpenAI, to support various aspects of the writing process, including improving clarity, grammar, spelling, and academic tone. All content generated with the assistance of this tool was carefully reviewed and edited by the authors, who take full responsibility for the final content of the manuscript.

References

1. Papa, T., Grillanda, N., and Milani, G. (2021). Three-dimensional adaptive limit analysis of masonry arch bridges interacting with the backfill. Engineering Structures, 248, 113189. https://doi.org/10.1016/j.engstruct.2021.113189.

2. Cavuslu, M., and Ülger, T. (2025). Enhancing the seismic resilience of the Batıayaz masonry bridge, aftermath of 2023 Kahramanmaras¸ earthquakes, using iron and FRP clamp-dowel connectors in the arch: Failure tests and numerical modelling. Engineering Failure Analaysis, 175, 109544. https://doi.org/10.1016/j.engfailanal.2025.109544

3. Kaya, A., Adanur, S., Bello, R.A., Genç, A.F., Okur, F.Y., Sunca, F., Altunisik, A.C., and Sevim, B. (2023). Post-earthquake damage assessments of unreinforced masonry (URM) buildings by shake table test and numerical visualization. Engineering Failure Analysis. 143, 106858. https://doi.org/10.1016/j.engfailanal. 2022.106858 34

4. Kaya, A., Roudane, B., Adanur, S., Sunca, F., Genc, A.F., Gunaydin, M., and Altunisik, A.C. (2024). Structural response of half-scale pumice concrete masonry building: shake table/ambient vibration tests and FE analysis. Meccanica, 59, 1159–1190. https://doi.org/10.1007/s11012-024-01849-4

5. Cavuslu, M., and Ülger, T. (2025). Seismic failure assessment of a 19th-Century masonry minaret with and without iron clamp and dowel Retrofit: Experimental Testing, ambient

vibration validation and numerical modeling. Engineering Failure Analaysis, 182, 110006. https://doi.org/10.1016/j.engfailanal.2025.110006

6. Castori, G., Borri, A., and Corradi, M. (2016). Behavior of thin masonry arches repaired using composite materials. Composites Part B, 87, 311-321. http://dx.doi.org/10.1016/j.compositesb.2015.09.008

7. Kocaman, I., and Gürbüz, M. (2024). Enhancing seismic performance of historic mosques through retrofitting measures. Engineering Structures, 301, 117245. https://doi.org/10.1016/j.engstruct.2023.117245

8. Cosgun, T., Ceylan, O., Nasery, M.M., Güler, Ö., Sayin, B., Uzdil, O., and Akcay, C. (2023). Seismic performance assessment and retrofitting proposal for a historic masonry school building (Bursa, Türkiye). Case Studies in Construction Materials, 18, e02087. https://doi.org/10.1016/j.cscm.2023.e02087

9. Corradi, M., Castori, G., and Adkins, J. (2026). Titanium ties for the reinforcement and repair of masonry constructions: Experimental and numerical investigation. Construction and Building Materials, 523, 146248. https://doi.org/10.1016/j.conbuildmat.2026.146248

10. Tanriverdi, S., and Yavuz, C. (2023). Investigation of the effects of clamp depths on the flexural behavior of walls in masonry walls. Construction and Building Materials, 393, 132081. https://doi.org/10.1016/j.conbuildmat.2023.132081

11. Akin, S.K., and Boztaş, M. (2024). Examining Mechanical Properties of Strengthened Aerated Concrete Masonry Walls. Case Studies in Construction Materials, 20, e02804. https://doi.org/10.1016/j.cscm.2023.e02804

12. Cavuslu, M., and Ulger, T. (2024). Impacts of the mechanical connectors on seismic performance of the restored masonry Plaka Bridge using experimental and numerical studies. Structures, 68, 107058. https://doi.org/10.1016/j.istruc.2024.107058

13. Sallam, M.A., Hassan, H.M., Sayed, M.A., Abdel Hafiez, H.E., Zahra, H.S., and Salem, M. (2023). Seismic vulnerability assessment of historical minarets in Cairo. Geoenvironmental Disasters, 10, 30. https://doi.org/10.1186/s40677-023-00260-7

14. Aymelek, A., Yanik, Y., Demirtaş, B., Yildirim, O., Çalik, I., and Türker, T. (2023). Full-scale structural evaluations of İskenderpaşa minaret. Structures, 55, 1028-1044. https://doi.org/10.1016/j.istruc.2023.06.055

15. Nasery, M.M. (2026). Innovative strengthening techniques for the 1300-Year-Old Harran Grand Mosque minaret severely damaged in the February 6, 2023 Kahramanmaraş earthquakes (Mw 7.7 and Mw 7.6). Engineering Failure Analysis, 183, 110268. https://doi.org/10.1016/j.engfailanal.2025.110268Get rights and content

16. Schiavoni, M., Roscini, F., and Clementi, F. (2025). Comparative analysis between continuous and discontinuous methods for the assessment of a cultural heritage structure. Meccanica, 60, 1957-1982. https://doi.org/10.1007/s11012-024-01885-0

17. Schiavoni, M., Di Giosaffatte, M., Roscini, F., and Clementi, F. (2026). Mechanisms detection by nonlinear finite and distinct element simulations of a historical religious masonry complex. Bulletin of Earthquake Engineering, 24, 2615-2659. https://doi.org/10.1007/s10518-025-02125-w

18. Schiavoni, M., Giordano, E., Roscini, F., and Clementi, F. (2023). Numerical Assessment of Interacting Structural Units on the Seismic Damage: A Comparative Analysis with Different Modeling Approaches. Applied Sciences, 13, 972. https://doi.org/10.3390/app13020972

19. Schiavoni, M., Giordano, E., Roscini, F., and Clementi, F. (2023). Numerical modeling of a majestic masonry structure: A comparison of advanced techniques. Engineering Failure Analysis, 149, 107293. https://doi.org/10.1016/j.engfailanal.2023.107293

20. Altunişik, A.C., Öztürk, M.M., Genç, A.F., Günaydın, M., Kaya, A., Akbulut, Y.E., and Sunca, F. (2024). Dynamic characteristics changes of masonry arches exposed to elevated temperature. Construction and Building Materials, 418, 135423. https://doi.org/10.1016/j.conbuildmat.2024.135423

21. Ural, A., and Uslu, S. (2014). Shear tests on stone masonry walls with metal connectors. European Journal of Environmental and Civil Engineering, 18(1), 66-86. https://doi.org/10.1080/19648189.2013.845857

22. Akin, S.K., and Boztaş, M. (2024). Examining Mechanical Properties of Strengthened Aerated Concrete Masonry Walls. Case Stıdies in Construction Materials, 20, e02804. https://doi.org/10.1016/j.cscm.2023.e02804

23. Kiral, A., Ergün, M., Tonyali, Z., Artar, M., and Sentürk, I. (2024). A case study comparing seismic retrofitting techniques for a historically significant masonry building's minaret, Engineering Failure Analysis, 166, 108873.

24. Asaad, R., and Kaadan, A. (2024). Retrofitting Existing Masonry Structures by Using Seismic Base Isolation System. Arabian Journal for Science and Engineering, 49, 5243-5254. https://doi.org/10.1007/s13369-023-08381-9

25. Gandolfi, A., Pingaro, N., and Milani, G. (2024). Simple Nonlinear Numerical Modeling for Unreinforced and FRP-Reinforced Masonry Domes. Buildings, 14(1), 166. https://doi.org/10.3390/buildings14010166

26. Wang, Z., Li, L., Zhou, J., Chen, R., Leng, J., Zhang, H., and Yang, J. (2024). Experimental investigation and calculation method of the interfacial bonding performance of stone masonry reinforced with UHPC. Journal of Building Engineering, 85, 108435, https://doi.org/10.1016/j.jobe.2024.108435.

27. Zampieri, P., Piazzon, R.,Niero, L., Pellegrino, C. (2024). Damaged masonry arch bridges strengthened with external post-tensioning: experimental and numerical results. Engineering Structures, 318, 117929. https://doi.org/10.1016/j.engstruct.2024.117929.

28. Kaminski, T., and Costa, C. (2024). Evaluation of strengthening efficiency based on combined global and sectional response of masonry arch bridges, Engineering Structures, 302, 117359. https://doi.org/10.1016/j.engstruct.2023.117359.

29. Shabani, A., and Kioumarsi, M. (2023). Seismic assessment and strengthening of a historical masonry bridge considering soil-structure interaction. Engineering Structures, 293, 116589. https://doi.org/10.1016/j.engstruct.2023.116589.

30. Yang, J., Wang, Y., Zhang, Z., Zou, Y., and Zhou, J. (2023). Early-age shrinkage characteristic of UHPC in strengthening stone masonry arch: influence of restraint from arch. Structure. Structures, 58, 105465. https://doi.org/10.1016/j.istruc.2023.105465

31. Xia, J., Yang, J., Zhang, Z., Zou, Y., Zhou, J., Wang, Z., Shen, X., and Kuang, Y. (2024). Evaluating the performance of masonry arch strengthened with UHPC at extrados and intrados by experimental, numerical and analytical approaches. Structures, 65, 106687. https://doi.org/10.1016/j.istruc.2024.106687.

32. Pantò, B., Ortega, J., Grosman, S., Oliveira, D.V., Lourenço, P.B., Macorini, L., and Izzuddin, B.A. (2024). Advanced calibration of a 3D masonry arch bridge model using non-destructive testing and numerical optimisation. Construction and Building Materials, 438, 137131. https://doi.org/10.1016/j.conbuildmat.2024.137131.

33. Ambrisi, A.D., Focacci, F., Luciano, R., Alecci, V., and Stefano, M.D. (2015). Carbon-FRCM materials for structural upgrade of masonry arch road bridges. Composites Part B: Engineering, 75, 355‑366. https://doi.org/10.1016/j.compositesb.2015.01.024

34. Yang, S.D., Zhao, L.D., Qiao, Q.Y., Liu, H.B., and Cao, W.L. (2025). In-plane seismic retrofitting of damaged masonry walls using steel components and polymer modified cement mortar strips. Construction and Building Materials, 487, 142022. https://doi.org/10.1016/j.conbuildmat.2025.142022

35. Kheirollahi, M., Chenaghlou, M.R., and Clobes, M. (2025). Seismic vulnerability assessment and retrofitting of the tabriz historical bazaar - a numerical and experimental investigation. Journal of Building Engineering, 112, 113418. https://doi.org/10.1016/j.jobe.2025.113418.

36. Contrafatto, L., and Cosenza, R. (2014). Behaviour of post-installed adhesive anchors in natural stone. Construction and Building Materials, 68, 355-369. http://dx.doi.org/10.1016/j.conbuildmat.2014.05.099

37. USGS. 2000. Implications for Earthquake Risk Reduction in the United States from the Kocaeli, Turkey, Earthquake of August 17, 1999. U.S. Geological Survey Circular 1193, p. 3. Denver, CO: U.S. Government Printing Office.

38. AFAD, Disaster and Emergency Management Presidency, 2024.

39. TADAS: Turkish Accelerometric Database and Analysis System. Available from: https://tadas.afad.gov.tr/

40. TBEC-2018, (Turkish Building Earthquake Code), Specifications for buildings to be built in seismic areas. Ministry of Public Works and Settlement, Ankara, Turkey.

41. Thamboo, J., Corradi, M., and Pologanathan, K. (2024). Investigating the mechanical characteristics of unreinforced and reinforced stone masonry using an Experimental database. Bulletin of Earthquake Engineering, 22, 2173-2199. https://doi.org/10.1007/s10518-023-01847-z

42. GMEHRS (2017) Guidelines for the Management of Earthquake Risks for Historical Structures. General Directorate of Foundations. Ankara, Turkiye.

43. Tomazevic M. Earthquake-Resistant Design of Masonry Buildings 1999;1. 10.1142/P055.

44. ASTM. (2013). "Standard test method for rock bolt anchor pull test." ASTM D4435-13e1, West Conshohocken, PA.

45. Roudane, B., Kaya, A., and Adanur, S. (2026). Nonlinear seismic damage analysis of low-rise masonry buildings using different materials. Engineering Failure Analysis, 184, 110287. https://doi.org/10.1016/j.engfailanal.2025.110287

46. ISO 6892-1:2019 (en), Metallic materials -Tensile testing - Part 1: Method of test at room temperature

47. Roscini, F., Nerilli,F., Ferracuti, B., and Guadagnini, M. (2025). Experimental and numerical investigation of the bond interface between basalt fibre and mortar in TRM system. Construction and Building Materials, 487, 142064. https://doi.org/10.1016/j.conbuildmat.2025.142064

48. Abdulla, K.F., Cunningham, L.S., and Gillie, M. (2017). Simulating masonry wall behaviour using a simplified micro-model approach. Engineering Structures, 151, 349-365.

49. Nasery, M.M. (2023). Investigating of the Reasons for the Collapse on the Entrance Arches of the Harran Grand Mosque (Ulu Cami) During the Kahramanmaraş Earthquakes (Mw 7.7 and Mw 7.6). Civil Engineering Beyond Limits, 3(1876).

50. Federal Emergency Management Agency (FEMA), Prestandard and Commentary for the Seismic Rehabilitation of buildings (FEMA 356), Federal Emergency Management Agency, Washington, D.C., 2000.

51. İzol, R., Bayrak, O.F., Ilki, A., Lourenco, P.B., Avcil, F., and Altunisik, A.C. (2025). Seismic behavior of historic square cross-section masonry minarets: The minaret of the Harran Ulu Mosque in Şanliurfa (Türkiye). Structures, 82, 110504. https://doi.org/10.1016/j.istruc.2025.110504

52. EN 1504-6, 2006. Products And Systems for the Protection and Repair of Concrete Structures - Definitions, Requirements, Quality Control and Evaluation of Conformity - Part 6: Anchoring Of Reinforcing Steel Bar. CEN, Brussels.